Alma Mater Studiorum – Università di Bologna

DOTTORATO DI RICERCA IN

Chimica Industriale

Ciclo XXIII

Settore/i scientifico-disciplinare/i di afferenza:
CHIM/04 CHIMICA INDUSTRIALE

The interaction of hydrocarbons with heterogeneous materials and catalysts: two examples of industrial interest

Presentata da:

Elisa Degli Esposti

Coordinatore Dottorato
Prof. Fabrizio Cavani

Relatore
Prof. Fabrizio Cavani

Esame finale anno 2011

Index

Pag.

1. MSA: history, production, properties, market

1.1 Zeolites: general aspects

Zeolites are aluminosilicates minerals. Their crystalline structure is made up by tetrahedral species TO_4 (T = Si, Al) in which oxygen atoms are shared between neighbour units. In this way non–linear oxygen bridges (angles range between 125 and 180 degrees) give rise to a regular porous structure with reversible adsorption properties for molecules like water or hydrocarbons.

SiO_4 species are electronically neutral when linked in a 3D frame work (e.g. quartz). Substituting Si(IV) with Al(III) in tetrahedra gives rise to a negative charging of the framework directly dependent on the number of AlO_4 species. Therefore, the structure is completed by extraframework cations electrostatically bounded that neutralize negative charges.

Zeolites possess a microporosity directly given by their crystalline structure. This peculiar property and the already mentioned extraframework cations allow zeolite to reversibly adsorb a wide range of molecules, from water to organics like hydrocarbons.

We can write a general formula for zeolites:

$$M_{x/n}[(AlO_2)_x(SiO_2)_y]\cdot mH_2O$$

where the cations (M) have a valence equal to n.

The name itself gives account to their adsorbing and desorbing properties: it was coined by the Swedish mineralogist A. F. Cronstedt in 1756 when he noticed that a

heated zeolite releases gaseous water. Hence the name “zeolite”, which in ancient Greek stands for “boiling stone”

In zeolites TO_4 units build up rings. The most common rings are 4-, 5- and 6-member rings. Many zeolites are based on β-cage unit, or sodalite unit (fig. 1), a truncated octahedron made up by 24 tetrahedral units. This b-cages build up complex frameworks with specific cavities for every zeolite. The resulting structure, whatever it is, is highly symmetric and posses channels that run parallel to x, y, z axis (fig. 2).

For example, in sodalite we have an inner cavity defined by eight sodalite units which a sodalite cage itself.

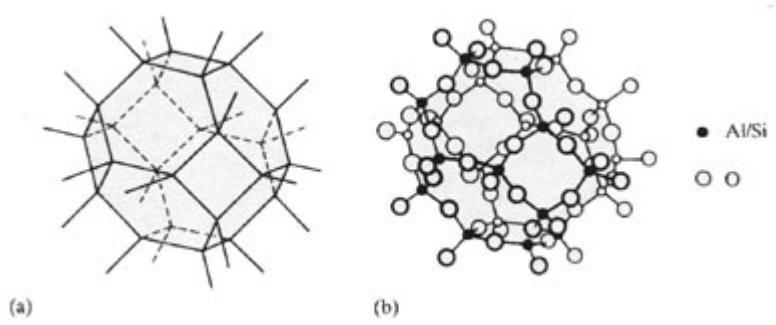

Fig. 1: sodalite unit (β-cage)

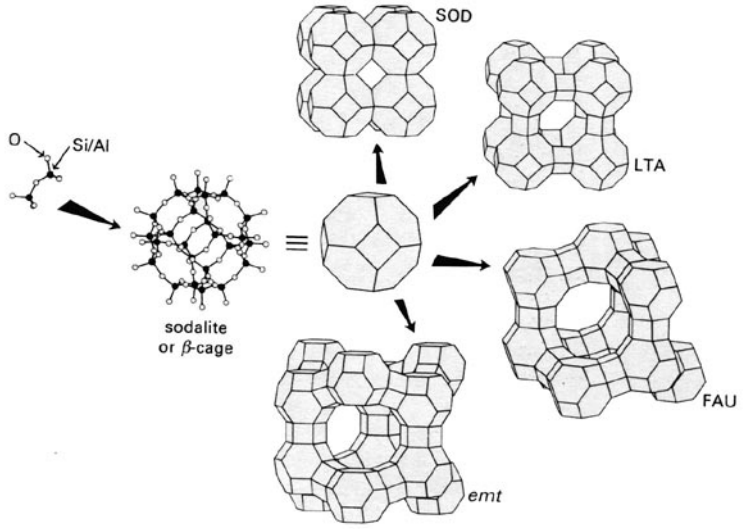

Fig. 2: different types of zeolites

1.2 Linde Type A zeolite (MS-nA)

Among other zeolites presented as examples in the figure we can see a synthetic zeolite, the Linde type A (fig. 3) (LTA according to the IZA)

In this zeolite sodalite units are linked by oxygen bridges between 4-member rings, making truncotahedral inner cavities (fig. 4) bigger than the sodalite ones (α-cage)[1, 2].

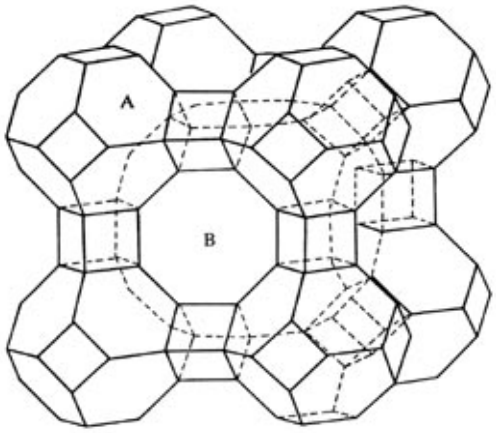

Fig. 3 LTA pore structure

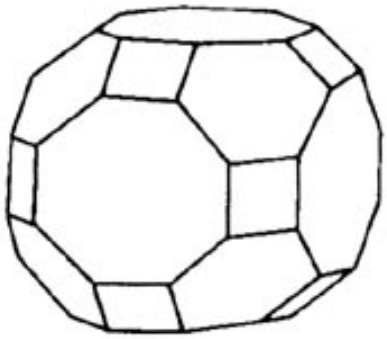

Fig. 4: LTA α-cage

LTA formula is $Na_{12}[(SiO_2)_{12}(AlO_2)_{12}]\cdot 27\ H_2O$. Si/Al ratio is 1:1 and the two elements are regularly alternated in the framework. This is an unusually high ratio, leading to a highly charged framework, thus to a high number of exchangeable extraframework cations and a higher hydrophilicity and in general an affinity towards polar molecules.

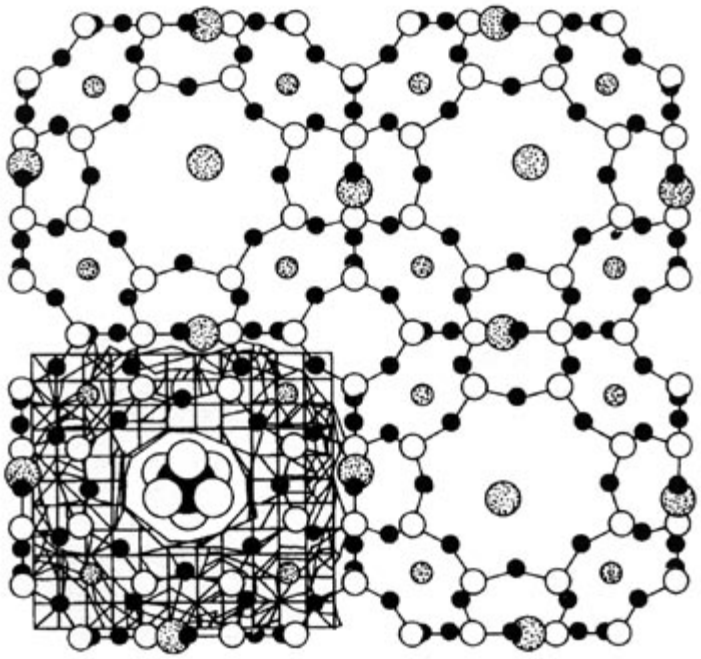

Fig. 5: K-LTA framework and different positions K^+ countercations may occupy in it

Cations may have different positions with respect to the framework. In figure 5 we present as examples different positions of cations in K-LTA. As we can see, some of them find place at the pore opening, other inside the α-cage.

Due to this peculiar flexibility in the type and positions of extraframework cations, in zeolites the dimensions of chan-

nels and pore entrance can be tuned modifying by ionic exchange the number and type of these species.

In this way we can select molecules of which dimensions are allowed inside and outside the pores and the environment they may find inside the zeolite. The relatively small pore size of LTA α-cage and the high number of cation required to its electronic neutrality make this type of zeolite particularly sensible and suitable for this kind of properties tuning.

LTA zeolites may have different countercations formulations, giving rise to different pore widths. Since they are widely used as water adsorbents and in separation process they are usually noted as Molecular Sieves (MS). An alpha-numerical code shows the pore width in Angstrom. The most common form of LTA zeolite is the Na-LTA (MS-4A), where all the countercations are Na^+ ions and the pore diameter is around 4 Å. These ions can be substituted with a lot of different ions, but mainly we find three different LTA zeolite formulations: K-LTA (i.e. MS-3A), Na-LTA and Ca, Na-LTA (i.e. MS-5A). In the last case the ionic exchange is not complete therefore we still have a percentage of Na^+ ions in the material.

Exchanging Na^+ ions with K^+ ions leads to a smaller pore opening due to the higher ionic radius of K^+. The pore opening is reduced to about 3 Å and the zeolite is suitable mainly as desiccant.

Ca, Na-LTA, on the other hand, by exchanging part of its monovalent ions with divalent ions decrease the total number of ions, creating more free space inside the framework. Furthermore, divalent ions choose as preferential adsorption sites inner cavities, leaving free access the pore.

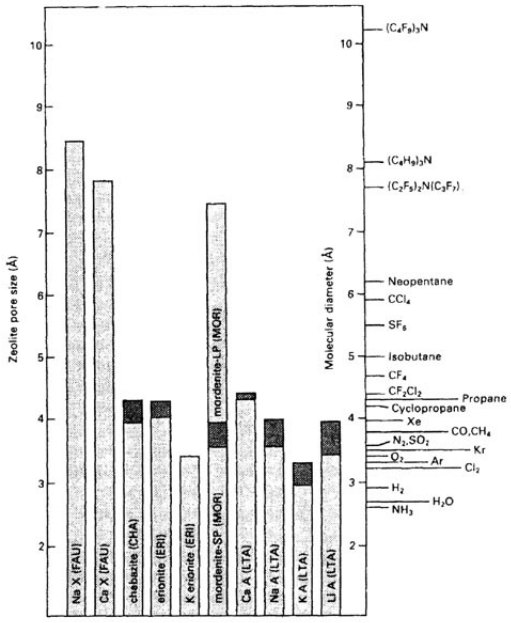

Fig. 6 Comparison between zeolite pore sizes and common molecular species

Zeolite pore size is compared with some molecular species diameter (see fig. 6). Molecular species diameters have been determined by kinetic measures. Darker blocks in the diagram represent the pore diameter increase caused by a temperature increase in the 77-420 K range.

1.3 LTA: ways of synthesis

Zeolite A, like other zeolites, is synthesized in a gelling process. Sources of alumina (usually sodium aluminate) and silica (usually sodium silicate) are mixed in basic aqueous solution to give a gel. The alkali agent can be NaOH or solutions of quaternary ammonium salts, amines, or other polar organics. The gel is then heated to 70-300ºC

to crystallize the zeolite. The zeolite is normally synthesized in the Na^+ form [3, 4].

Also different raw materials can be used, like kaolinite used as it is [5] or after an alkaline fusion prior to hydrothermal reaction [6].

In the last ten years much interest and research efforts have been directed toward zeolite membranes [7] thanks to the outstanding performances in separation processes and the advantages linked to their use in industrial large scale plants.
This brought an impulse toward the study of new way of synthesis, in particular by microwave heating [8, 9].

There are even some proposal for manufacturing low-grade zeolites from fly ash for fertilizer applications [11].

1.4 LTA applications [10]

The largest single use for zeolite is the global laundry detergent market, as water softener. This amounted to 1.44 million metric tons per year of anhydrous zeolite A in 1992.

Zeolites A considerably raises the cation exchange capability of soil making them suitable for agri/horticultural applications [11]. Zeolite freely exchange certain plant nutrients, significantly improving fertilizers utilization. Cation nutrient ions, such as calcium magnesium, potassium, sodium and particularly ammonia are exchanged in this way.

Zeolite A is of much interest because its supercage structure is useful in shape-specific catalysis. The inner cavity is large enough for structure changing reactions to take place, but the small pore means only a specific

structure can get into the cavity for reaction, typically n-paraffins and olefins. One use is in paraffins cracking. The hydrogen forms of zeolites (prepared by ion-exchange) are powerful solid-state acids, and can facilitate a host of acid-catalyzed reactions, such as isomerisation, alkylation, and cracking. Furthermore the small entry pore is selective towards linear paraffins, and cracking can occur on sites within the supercage (α-cage) to produce smaller chain alkanes. Zeolite A is also widely used in ion exchange separations [12] and gas separations.

2. Evaluation of n-hexane and water adsorption properties of MS-5A

2.1 Aim of the work

In the first part of this Ph.D. we focused on understanding the interactions that take place between MS-5A (Ca, Na-LTA) and n-hexane in an industrial application scenario. This means reproducing and monitoring by DRIFTS activation (dehydration) and adsorption procedures as close as we could to the process plant ones.

We develop a lab plant in order to develop a test procedure suitable for elucidating some dynamics of adsorption and desorption.

As last thing, we tried to highlight some correlations between adsorption data, spectroscopic data and Ca^{2+} percentage in samples.

2.2 Ca, Na-LTA: synthesis

First of all, we needed to obtain MS-5A samples with a wide range of Ca^{2+} percentages in order to explore how this parameter influences water and hexane adsorption performances.

As mentioned in chap. 1, LTA zeolite is usually synthesized in its Na-form and then undergoes a procedure of ionic exchange. Our first attempts of synthesis followed standard industrial procedures, mainly based on a large excess of Ca^{2+} ions source (of $CaCl_2 \cdot 6H_2O$), boiling temperature of the medium (water) and a long time of exchange (60 minutes). After the ex-

change was complete, samples were filtered, washed with demineralized water and dried at 378 K overnight.
This procedure didn't allow us to obtain samples that depart from industrial usual values of Ca^{2+} substitution percentage (70%-85%).

In the light of the great affinity showed by Na-LTA towards the substitution with Ca^{2+}, we develop a different procedure in which a stechiometric amount of Ca^{2+} source is used, at water boiling temperature, for 5 minutes.
All the other phases (cooling under stirring, vacuum filtering, double cake washing with demineralized water, overnight drying at 120°C) were kept without changes.

In this way we obtained four Ca, Na-LTA samples in which 27%, 50%, 63% and 72% of the Na^{+} cations were exchanged with Ca^{2+} ions, denoted respectively as UBo27, Ubo50, UBo63 and UBo72 in addition to non-exchanged Na-LTA denoted UBo00.
Ca^{2+} exchange percentages were confirmed by ICP analysis.

For all the experiments, zeolites were pressed and then manually granulated and sieved 40-60 mesh.

2.3 n-hexane adsorption equipment

To carry adsorption test on samples we modified a GC embedding a cylindrical sample holder inside the oven. It was fed by a flux of n-hexane in N_2 (inert gas carrier) and outputs were monitored by the FID detector of the GC.

By a valve system it was possible to send to the reactor a feed of carrier gas during the outgassing and de-

hydration step and then to switch to n-hexane in carrier gas during the adsorption test.

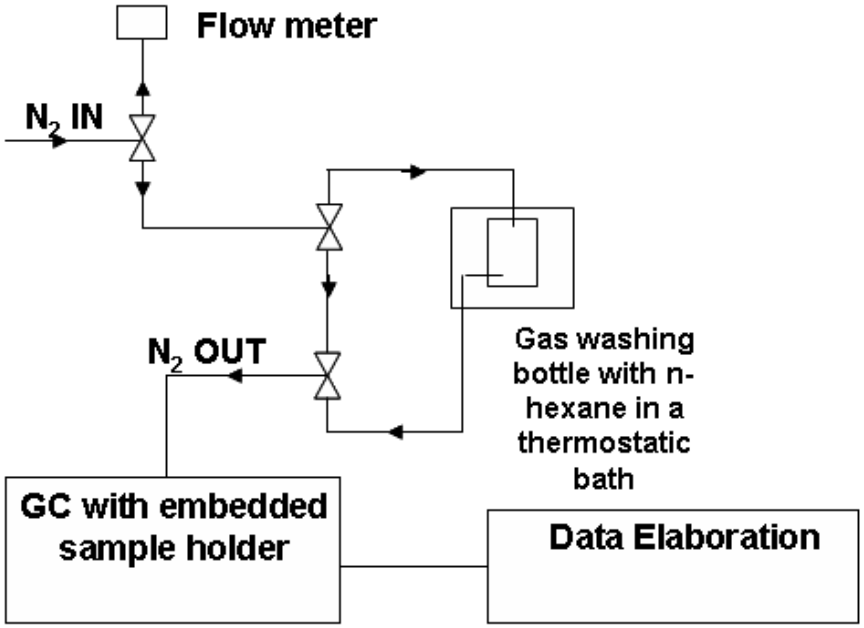

Fig. 7: Adsorption test apparatus scheme.

Each test was conducted over a carefully weighted amount of granulated sample. The first step was dehydration: the sample was heated to 623 K with a 20 K/min thermal program, then kept at 623 K for 30 minutes.

Then an adsorption test was conducted at 323 K: n-hexane feed is sent to the sample holder, the sample is held at the adsorption temperature, monitoring by FID the amount of hexane not adsorbed. When that quantity reaches a plateau remaining stable for some minutes the feed is switched to N_2 and a thermal programmed desorption starts (20 K/min) up to 573 K. The highest temperature is maintained until all hexane desorbed.

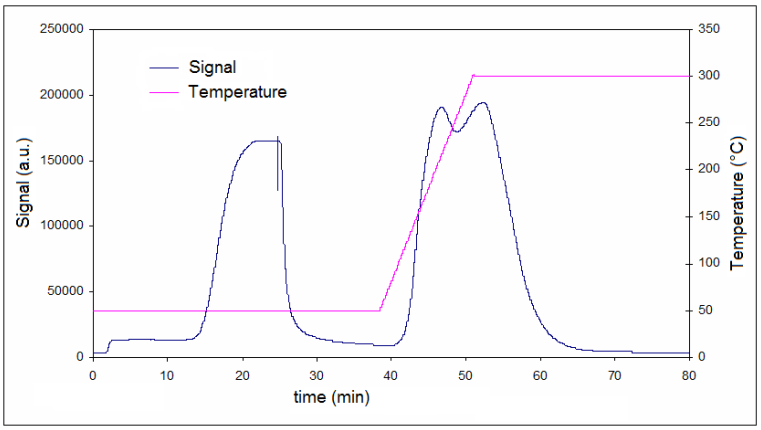

Fig. 8: a typical chromatogram from an adsorption test. Around 24 min the switch to inert carrier gas after adsorption plateau is marked.

The amount of n-hexane fed to the system was calculated from N_2 flux (25 ml/min) and the temperature of the liquid n-hexane (268 K) inside the gas washing bottle.

Since hexane is desorbed at a different temperature from the adsorption temperature using the same correlation factor can lead to relevant errors in data evaluation. Thus the amount of n-hexane desorbed by the sample was calculated subtracting the area of adsorbed hexane (considering also the dead volume of the system) to what should be the theoretical rectangular area of n-hexane fed in absence of an adsorber (the sample)

Area of desorbed hexane = zone 1 – zone 2 – zone 3

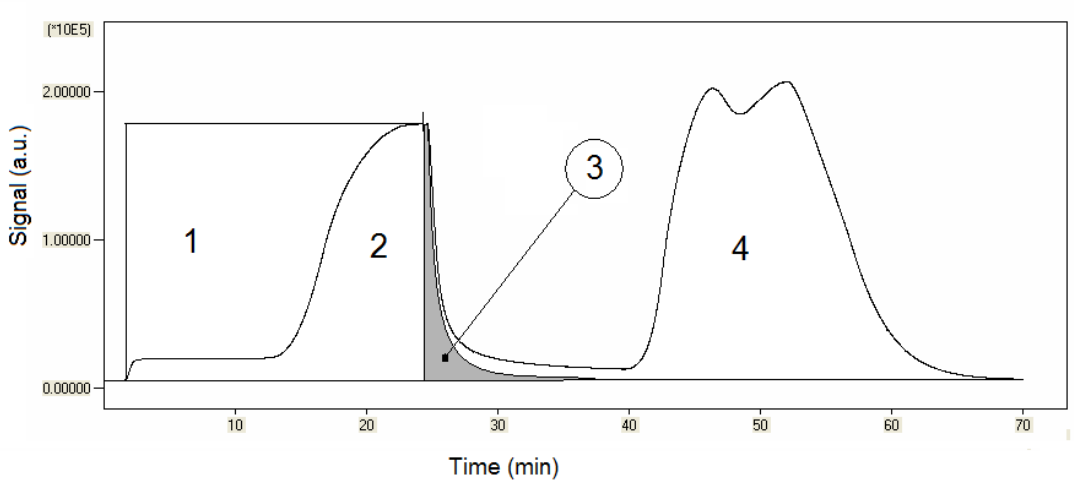

Fig. 9: zone 1: theoretical area of n-hexane fed in absence of an adsorbers; zone 2: area of adsorbed hexane; zone 3: system dead volume; zone 4: desorbed hexane (at a different T from the adsorption temperature)

2.4 n-hexane adsorption results and discussion

We could elucidate that below a certain pore diameter n-hexane cannot penetrate into zeolitic channels. (See Table 1).

Table 1. Summary of hexane adsorption results

Sample	g of n-hexane per 100g of sample
UBo00	No adsorption
UBo27	No adsorption
UBo50	4.17
UBo63	6.54
UBo72	7.58

In LTA available pore diameter for molecules is tuned by the percentage of countercationic substitution with respect to the sodium form [13]. MS-4A pore diameter is not large enough to allow n-hexane molecules to penetrate into the zeolite, and also a 27% sodium substitution doesn't give rise to significant adsorptions.

UBo50 shows a limited adsorption, not suitable for industrial applications. On the contrary, UBo63 and UBo73, whose substitution percentages are closer to the industrial ones, show growing adsorption values.

We can expect adsorption values growing up to a maximum, then going back to lower values for the highest substitution percentages (above 90%) due to the progressive blocking of the pores due to the Ca^{2+} concentration close to the Na^{+} one in MS-4A. [13]

Having the two cations comparable ionic radii we can thus expect high-Ca^{2+}-loading LTA zeolites having the same adsorption rate of Na-LTA ones.

2.5 DRIFTS measurements of water persistence

The DRIFT experiments were carried out with a Vertex 70 spectrometer (Bruker) using a diffuse reflection attachment equipped with a ZnSe-windowed reaction chamber (Pike), which allows temperature-programmed investigations between room temperature and 1173 K in a carrier gas flow (N_2 99.9995% supplied by SIAD).

We checked by DRIFT the “activation” (dehydration) of samples following an industrial-like procedure.

The sample is heated up to 623K (10 K/min), held at 623K for 60 minutes, then cooled down to 323K always under N2 flux.

After that we noticed that soma bands typical of water were still present and quite well defined.

Since the presence of other molecules can largely affect adsorption performances in zeolites, we decided to go deeper into the presence of a persistent hydration in our samples.

For each experiment on water persistence the sample cup was filled with overnight dried zeolite (granulated, 40-60 mesh). The samples were flushed with nitrogen at 323 K for 5 minutes and then the linear temperature program (10 K/min) was started.

Samples were held at 623 K for 60 minutes, then they were let to cool down to 323 K, and then they underwent to a second dehydration cycle since we verified that spectra recorded after a single dehydration cycle were not enough reproducible.

Spectra herewith discussed were recorded after the second activation cycle using a dried and outgassed KBr spectrum as reference.

Spectra were recorded with a resolution of 2 cm^{-1}, accumulating 256 scans.

2.6 DRIFTS water persistence measurements: results and discussion

Before dehydration, DRIFT spectra of all samples show a broad, almost featureless band in the hydroxyl combination bands region resulting irrelevant for the purpose of investigating the characteristic of a “persisting” hydration in zeolites in industrial conditions.

Therefore, we will discuss here the DRIFT spectra of zeolites at 323 K after two cycles up to 623 K, which is the most common industrial dehydration procedure temperature.

NIR spectra of samples are shown in fig. 10 and 11

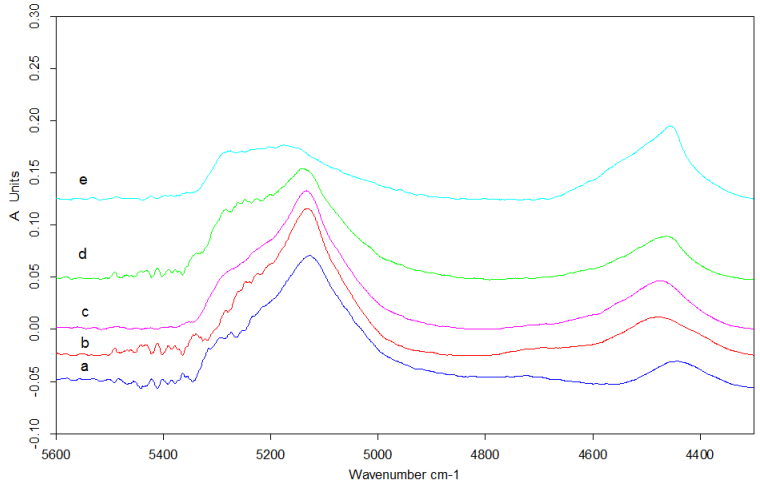

Fig. 10. DRIFT spectra in the NIR region: a: Ubo00; b: UBo27; c: UBo50; d: Ubo63;e: UBo72

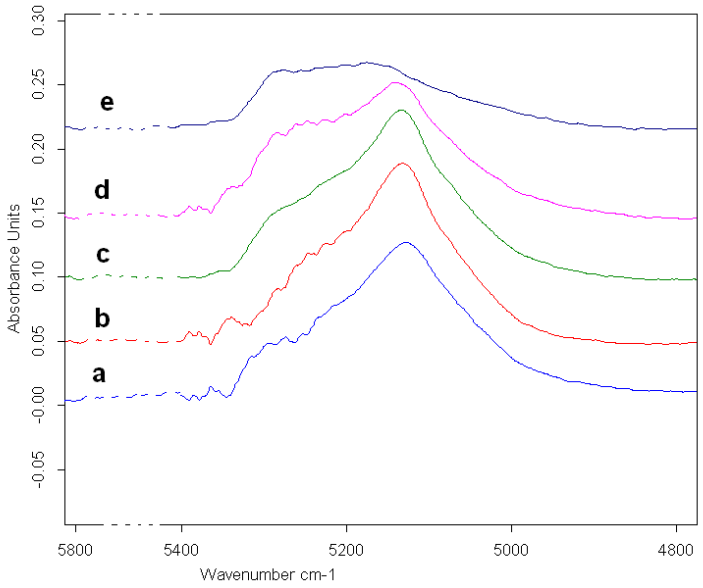

Fig. 11: DRIFT spectra of persistent water bands: a: Ubo00; b: UBo27; c: UBo50; d: Ubo63;e: UBo72

After the first cycle and after the second cycle band intensities don't change significantly, neither the shapes change.

Spectra show three main components: 5270-5280 cm^{-1} (water S2-coordinated, where both OH groups experience interactions of similar strength); 5140-5150 cm^{-1}: semi-liquid clusters of water; 4460-4480 cm^{-1}: combination band of stretching and bending modes of SiO-H groups. [14, 15, 16].

Since in the spectra there aren't bands above 5300 cm^{-1} we can exclude water molecules having weaker interactions with the zeolite (e.g. single

hydrogen interaction or interactions with the oxygen of the framework)
While the component around 5140 cm^{-1} is predominant in samples with a low Ca^{2+} content, the component at 5270 cm^{-1} changes from a shoulder to an intensity comparable with the main band's one.

Samples with low Ca^{2+} content show a very weak band around 4700 cm^{-1} that is no longer visible in other samples.

Silanols combination band loses more and more symmetry going toward high percentage of Ca^{2+} in the samples, probably due to electrostatic deformations inducted in Vibrational modes by a stronger charge density.

In the same way, H_2O bands progressively drift toward higher wavenumbers as the Ca^{2+} percentage increase.

We hypothesized that Water molecules in S2 coordination are interacting with the oxygen of silanols group living rise to the band at 5280 cm^{-1} and that water molecule organized in solvating clusters around Ca^{2+} ions give account to the band at 5140 cm^{-1}.
The ratio between the two bands could potentially be indicative of the real accessibility of silanols group and Ca^{2+} ions.

2.7 Empirical correlations

We considered some empirical parameter derived from band integration: S2/cluster ratio of water molecules, S2/total persistent hydration ratio and cluster/total persistent hydration ratio (fig. 12)

Spectra have been deconvoluted and integrated using OPUS software provided by Bruker [http://www.bruker.com/].

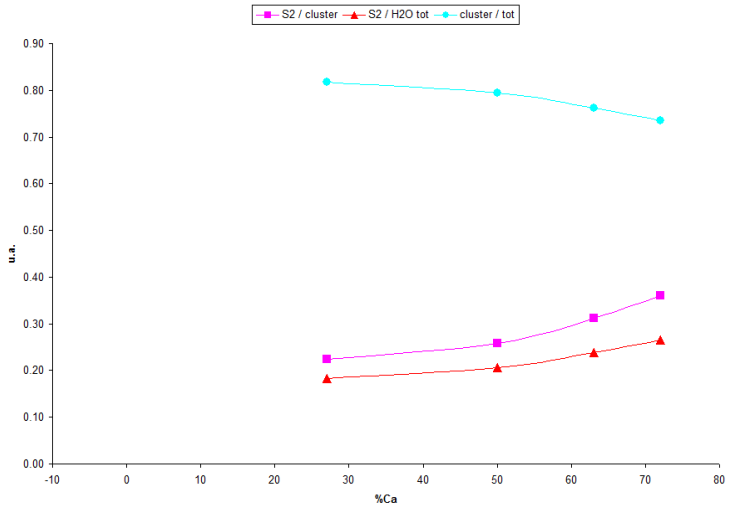

Fig. 12: correlations between Ca^{2+} loading and persistent water species for UBo samples.

A higher Ca^{2+} content leads to a relative growth of water molecules in S2 coordination with respect to semi liquid clusters in which water molecules are less interacting with the host material.

This can be linked with the increasing concentration of charge density we achieve in the material going from monovalent cations to bivalent cations:

thus, water is more strongly bind and is less mobile in cavities.

By the analysis of zeolite 4A, mostly used as desiccants, we can see that water specie distribution is close to the one observed in zeolites 5A with "industrial" Ca loading (around 70%). This can be explained considering that during the exchange a Ca^{2+} cation substitute two Na+ cations, thus giving a higher charge density from point to point but "diluting" the positive charged zones inside the zeolites. A 100% Na zeolite has a well distributed countercationic environment that leads to a relative high number of water molecule experiencing symmetrical interactions with the material.

2.8 DRIFTS n-hexane adsorption dynamics measurements

For each n-hexane adsorption experiment the sample cup was filled with overnight dried zeolite (granulated, 40-60 mesh). Each sample underwent two dehydration cycles according to the method described above before hexane adsorption was carried on.

After dehydration samples were held at 323 K under a flux of N_2, then a 60-seconds pulse of n-hexane in N2 was sent to the cell using an apparatus as close as possible to the adsorption lab plant described above. After the pulse N_2 was sent again to the sample and sample equilibration was followed by DRIFT spectroscopy. Spectra recording was started just after the end of the pulse were recor-

ded with a resolution of 4 cm^{-1}, accumulating 128 scans. A spectrum each 2 minutes was taken.

As reference, a spectrum of each sample recorded just before the pulse was used. After no more than 20 minutes all samples showed no further changes in spectra.

2.9 DRIFTS n-hexane adsorption dynamics measurements: results and discussion

Analyzing the DRIFT spectra taken during n-hexane adsorption we focused on three crucial spectral zones of n-hexane: stretching MIR region around 2900 cm^{-1} and NIR zones around 5800 cm^{-1} and 4340-4014 cm^{-1}.

Experimental bands in these three regions for gas-phase n-hexane are:

Wavenumbers (cm^{-1})	Attribution
2970	n C-H_3^{as}
2935	n C-H_2^{as}
2875	n C-H_3^{s}
5939	
5898	
5835	
5691	
4406	

4348	
4280	
4192	
4089	
4020	

No unambiguous attribution is given for NIR bands since they are combination bands involving various fundamental modes and sometimes their overtones.

What is important to highlight for the interpretation of our tests is that in gas phase hexane MIR bands are pretty strong, while NIR bands are very weak. In order to have appreciable intensities liquid solution of hexane and long optical path are required [17].

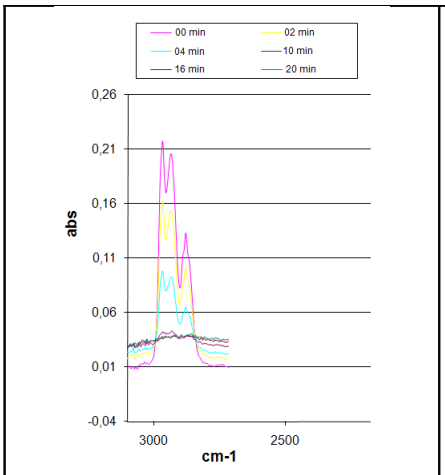

UBo27

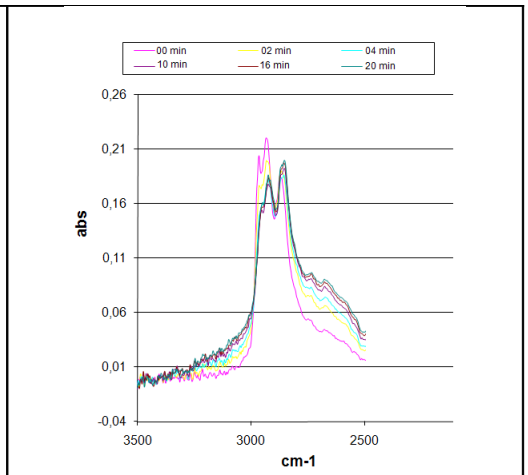

UBo50

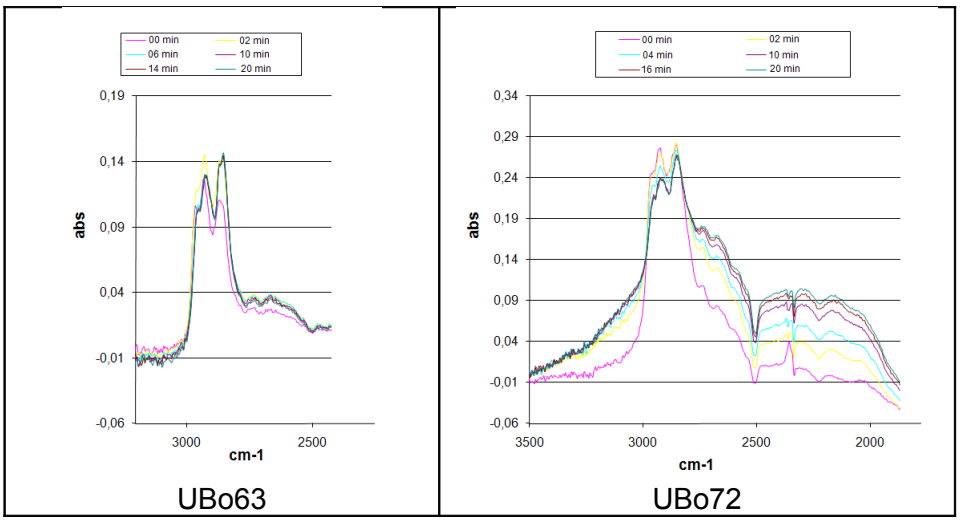

Fig. 13: MIR spectra of samples during purging after n-hexane adsorption

In figure 13 we present adsorption dynamics spectra taken in the MIR C-H_3 stretching region of hexane. For reference, we present also spectra taken with Na-LTA (fig. 14)

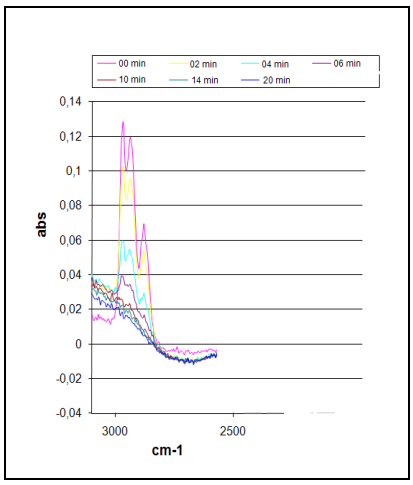

Fig. 14: MIR spectra of Na-LTA during purging after n-hexane adsorption

We can see that in Na-LTA hexane bands disappear soon after stopping the hydrocarbon feeding. Relative intensities of the three bands are similar to the one of gaseous hexane.

A similar dynamic is showed by UBo27, confirming that with a low percentage of Ca^{2+} substitution pores aren't large enough to allow n-hexane inside the zeolite. The hydrocarbon remains outside the material and is easily removed by purge flux.

Going toward higher substitution percentages we notice two things: hexane stretching bands don't decrease during the purge and relative intensities are strongly different from the one of the gas phase spectrum.

This means that hexane is effectively adsorbed inside the pores of the zeolite and a simple purge at low temperature can't remove it. Furthermore, this change in relative intensities suggest an interaction with the environment found inside the pore, stronger and stronger increasing the percentage of Ca^{2+}. The interaction deforms the molecules inside the zeolite, altering the symmetry they can have in gas phase, affecting in particular asymmetrical stretching bands.

In the NIR region, the spectra of the two significant zones are:

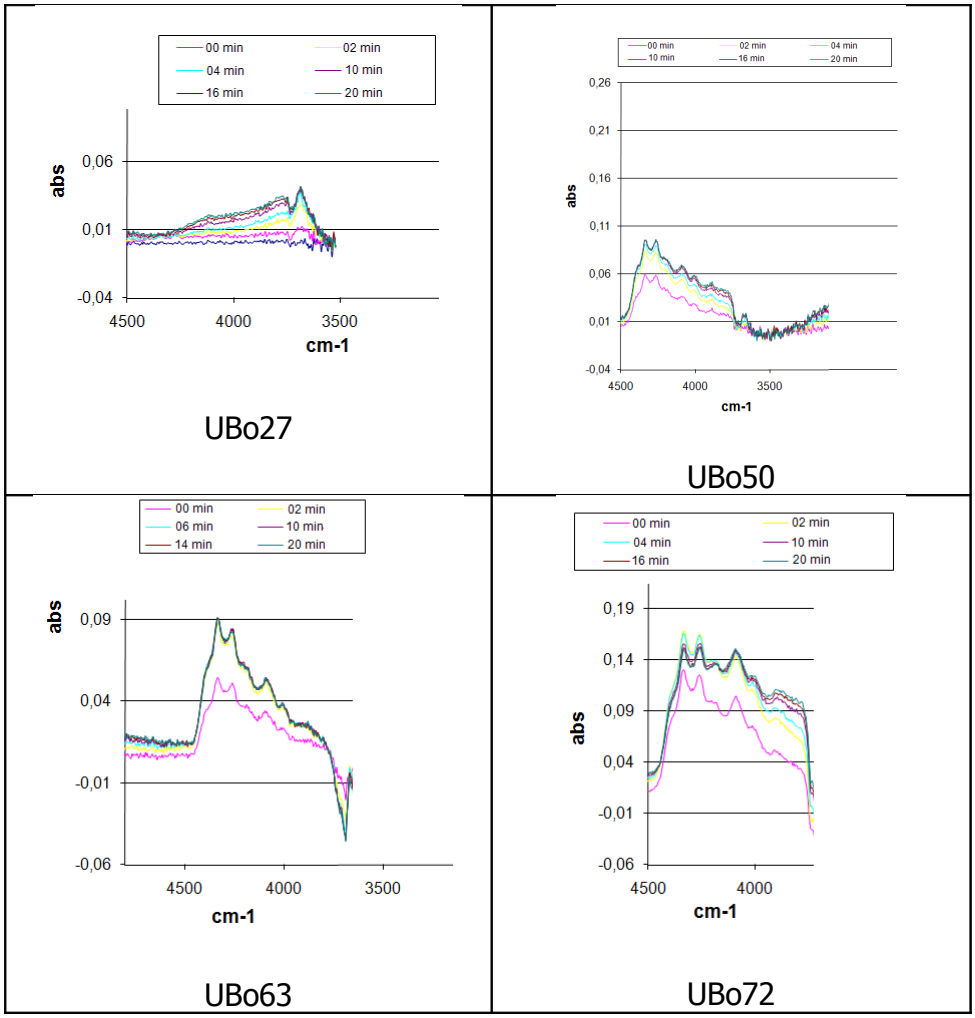

Fig. 15: NIR spectra (4500 – 3500 cm^{-1}) of samples during purging after n-hexane adsorption

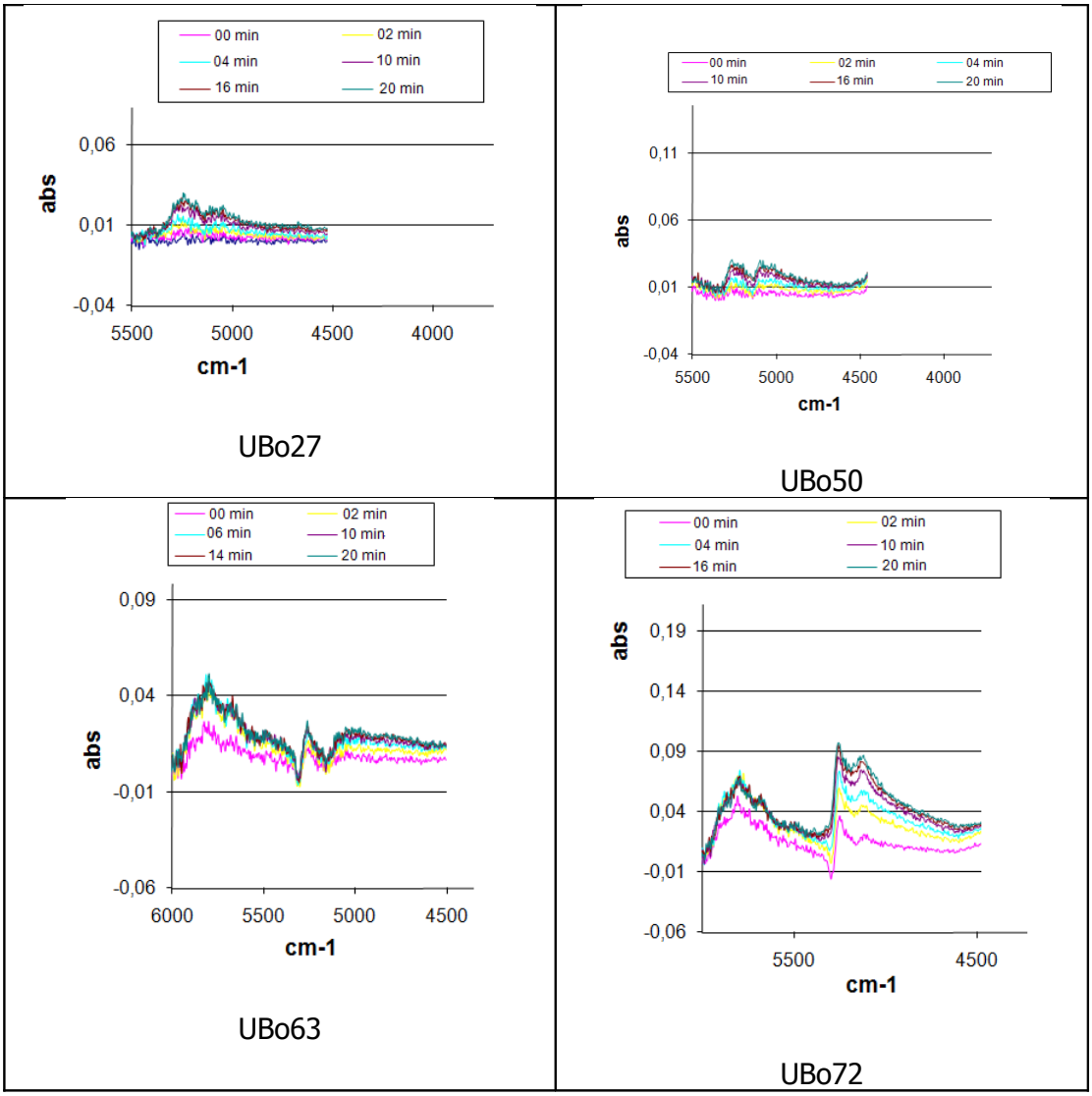

Fig. 16: NIR spectra (6000 – 4500 cm^{-1}) of samples during purging after n-hexane adsorption

As a reference we include the spectra taken with Na-LTA (fig. 17).

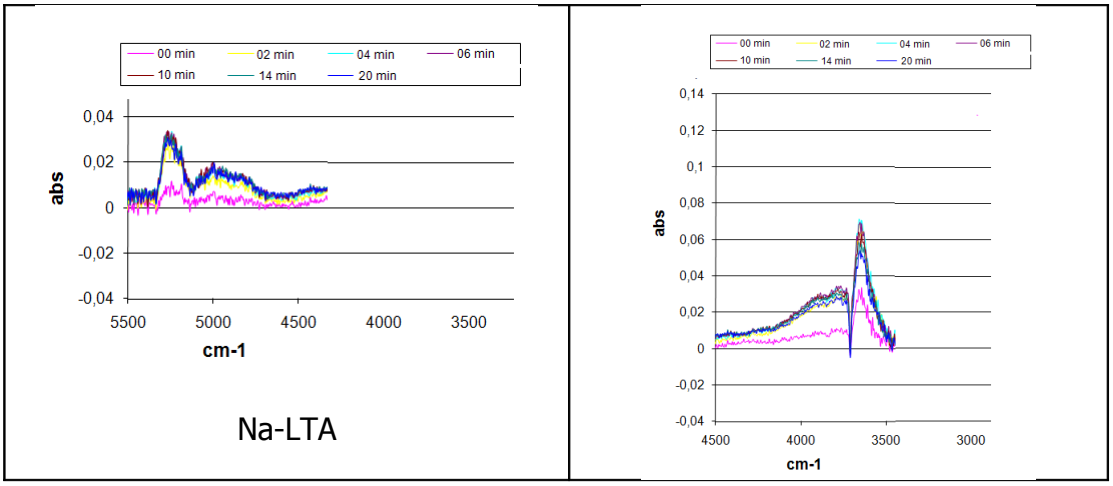

Fig. 17 NIR spectra (6000-4500 cm^{-1} and 4500 – 3500 cm^{-1}) of Na-LTA during purging after n-hexane adsorption

As above, samples with low Ca^{2+} percentage show no hexane adsorption, while are still quite visible the bands related to the persistent water inside the zeolite.

Sample with a good hexane adsorption show peaks shifted even for 10-20 cm^{-1} with respect to the gas phase. Furthermore, in our sample exposed to hexane NIR bands show intensities comparable with MIR ones. We explained this by supposing hexane condensing in a pseudo-liquid phase into zeolitic pores, therefore achieving a much higher concentration than in gas phase in the same optical path. [17]

3. Silver nanoparticles: synthesis, characterization and application in catalytic reactions

3.1 Aim of the work

In the second part of this Ph.D. we directed out attention to another type of material extremely promising for industrial chemistry: metallic nanoparticles.

In particular, we decided to focus on silver nanoparticles for many reasons:
Nanoparticles may exhibit size-related properties that differ significantly from those observed in fine particles or bulk materials [18, 19]
Gold has always been the main actor in NP chemistry, and only in very recent years researchers started to work on it as much as for gold
Silver is less expensive than gold, therefore it is more suitable for mass-scale application in catalysis and for a wider range of reactions
Metallic silver possess unique catalytic properties which make it often the only catalyst suitable for some reactions (see 3.3)

We planned to develop a green synthesis that could yield to nanoparticles suitable for being placed on a support in order to have a heterogeneous catalyst (for further considerations see 3.4). Then we tested it in an increasing important reaction of catalytic decomposition of soot.

We also had the possibility to run some tests at the synchrotron facility ELETTRA in Trieste, Italy. We ran ESCA experiments at the ESCAMicroscopy beamline testing the material in contact with reactive gases at various temperatures.

3.2 Metal nanoparticles: a brief overview

Nanoparticles have a very long history. They date back to mesopotamic artisans, which used them to create glittering effects on pots surface. This so called “luster” effect was used also in Middle Age and Renaissance pottery
This empirical refining of this technique probably took place among the Islamic artisans. As Muslims were not allowed to use gold in artistic representations, they had to find a way to create a similar effect without using real gold [20]. The luster originated within the film itself, which contained silver and copper nanoparticles dispersed homogeneously in the glassy matrix of the ceramic glaze. These nanoparticles were created by the artisans by adding copper and silver salts and oxides together with vinegar, ochre and clay, on the surface of previously-glazed pottery. The object was then placed into a kiln and heated to about 600 °C in a reducing atmosphere
Luster technique showed that ancient craftsmen had a rather sophisticated empirical knowledge of materials and confirms the debt of gratitude that modern chemistry should own to medieval Middle-Eastern alchemists.

Gold nanoparticles colloidal solutions were also stated in 5th-4th millennium B.C. in Egypt and China, used as tonics [21].

Furthermore, the very well known Lycurgus cup, a fine example of dicroic glass dated back to IV AD, uses silver and gold nanoparticles in the glass formulation to give rise to different colors depending if the light pass through the cup or it's just reflected (ruby red in transmitted light, green in reflected light).

Paracelsus (1493-1541), a pioneer of the use of chemicals and minerals in medicine, described a synthetic method for "aurum potable, oleum auri: quinta essentia auri" based on the reduction of $HAuCl_4$ by an alcoholic extracts of various plants.

Other physicians wrote about colloidal gold: here we mention Francisci Antonii in 1618 [ref. in 21] and Johann Kunckels in 1676.

The glass colorant "purple of Cassius" was very popular in the 17th century [ref. in 21] and it's a colloid resulting from the heterocoagulation of gold particles and tin dioxide.

Michael Faraday provided the first description, in scientific terms, of the optical properties of nanometer-scale metals in his classic 1857 paper [22].
In a subsequent paper, Turner [23] points out that: "It is well known that when thin leaves of gold or silver are mounted upon glass and heated to a temperature which is well below a red heat (~500 °C), a remarkable change of properties takes place, whereby the continuity of the metallic film is destroyed. The result is that white light is now freely transmitted, reflection is correspondingly diminished, while the electrical resistivity is enormously increased."

In the modern days nanoparticles are attracting more and more scientific interest as they are effectively a

bridge between bulk materials and atomic or molecular structures. Their properties are neither those of bulk material nor those of molecular compound. At the nano-scale size-dependent properties are often observed as the percentage of atoms at the surface of a material becomes significant. The interesting and sometimes unexpected properties of nanoparticles are therefore largely due to the large surface area of the material, which dominates the contributions made by the small bulk of the material.
Therefore the nanoparticles properties strongly depends on the particle size, interparticle distance, shape and nature and quantity of adsorbed molecules on them.

Nanoparticles often possess unexpected optical properties as they are small enough to confine their electrons and produce surface plasmon resonance. For example nanoparticles of usually yellow gold and gray silicon are red in color.

Also absorption of solar radiation in photovoltaic cells is much higher in materials composed of nanoparticles than it is in thin films of continuous sheets of material, i.e. the smaller the particles, the greater the solar absorption.

Other size-dependent property changes include quantum confinement in semiconductor particles and superparamagnetism in magnetic materials.

Moreover, nanoparticles have been found to impart some extra properties to various day to day products. For example the presence of titanium dioxide nanoparticles imparts what we call the self-cleaning effect (since they effectively catalyze the

decomposition of organic matter), and the size being nanorange, the particles cannot be observed. Zinc oxide particles have been found to have superior UV blocking properties compared to its bulk substitute. This is one of the reasons why it is often used in the preparation of sunscreen lotions [24], and is completely photostable [25].

Clay nanoparticles when incorporated into polymer matrices increase reinforcement, leading to stronger plastics, verifiable by a higher glass transition temperature and other mechanical property tests. These nanoparticles are hard, and impart their properties to the polymer (plastic). Nanoparticles have also been attached to textile fibers in order to create smart and functional clothing [26].

Metal, dielectric, and semiconductor nanoparticles have been formed, as well as hybrid structures (e.g., core-shell nanoparticles). Nanoparticles made of semiconducting material may also be labeled quantum dots if they are small enough (typically sub 10 nm) that quantization of electronic energy levels occurs. Such nanoscale particles are used in biomedical applications as drug carriers or imaging agents.

All these different properties from bulk material have to be well understood and made predictable since not always a “nano”-related property is desirable. For example, ferromagnetic materials smaller than 10 nm can switch their magnetization direction using room temperature thermal energy, thus making them unsuitable for memory storage [27].

Nanoparticles (e.g. gold ones) melt at much lower temperatures (~300 °C for 2.5 nm size) than their slabs (gold: 1064 °C) [28, 29].

Colloidal suspensions of nanoparticles are possible since the interaction of the particle surface with the solvent is strong enough to overcome density

differences, which otherwise usually result in a material either sinking or floating in a liquid.

Due to their high surface reactivity nanoparticles have to be stabilized by some stabilizing agents, usually organic polymers (but also thiols, silica and so on) that cover the whole surface of every particle avoiding reactions between them.

3.2.1 Potential health and environmental hazards

Nanomaterials, even when made of inert elements like gold, become highly active at nanometer dimensions. Nanotoxicological studies are intended to determine whether and to what extent these properties may pose a threat to the environment and to human beings.

Furthermore, their intrinsic potential to penetrate the skin poses some issues about the risks of contamination through the cutaneous route during production and use [30].

Nanostructures can activate the immune system inducing inflammation, immune responses, allergy, or even affect to the immune cells in a deleterious or beneficial way (immunosuppression in autoimmune diseases, improving immune responses in vaccines)

Size is therefore a key factor in determining the potential toxicity of a particle. However it is not the only important factor. Other properties of nanomaterials that influence toxicity include: chemical composition, shape, surface structure, surface charge, aggregation and solubility [31] and the presence or absence of

functional groups of other chemicals [32]. The large number of variables influencing toxicity means that it is difficult to generalize about health risks associated with exposure to nanomaterials – each new nanomaterial must be assessed individually and all material properties must be taken into account.

3.3 Ag^0 uses

3.3.1 Silver: historical and modern applications

Metallic silver is used everywhere around us in our everyday life, sometimes in important function without being noticed for this [33].

Traditional uses for silver are, apart from jewelry and tableware, in coinage (Until the late 19th century, most nations were on a silver standard with silver coins forming the main circulating currency. Although gold was also used in coinage, its higher value was not practical for everyday payments) and photography.
Because of the growth of digital photography, Silver-based photography (based on light striking sensitive silver-halide crystals suspended on a film and then the development of the negative into silver-imbedded paper has been steadily dropping for almost a decade. Nonetheless, because of its extreme accuracy and cost effectiveness, silver-halide films are still chosen for some applications. For example, medical X-Ray technicians, and, many motion picture makers still prefer silver- halide film over digital, because of its low cost, excellent resolution and true color properties.

Also many batteries are manufactured with silver alloys as the cathode or negative side. Although expensive, silver cells have power-to-weight characteristics superior to their competitors.
Furthermore, due to environmental and safety concerns, silver-oxide batteries are beginning to replace lithium-ion batteries in mobile phones and laptop computers. Silver-zinc batteries feature a water-based chemistry and contain no lithium or flammable liquids.

Silver facilitates the joining of materials - called brazing when done at temperatures above 600°C and soldering when below - and produces naturally smooth, leak-tight and corrosion-resistant joints.
Also silver electrocoates steel ball bearings are widely used in continuous, heavy-duty applications such as in jet engines.

Silver finds a wide application in electronics products Because of its excellent electrical conductivity.
Silver membrane switches, highly reliable and last for millions of on/off cycles
For printed circuit boards, used in consumer items from mobile phones to computers, silver-based inks and films are applied to composite boards to create electrical pathways. In similar fashion, silver-based inks produce so-called RFID tags.
Silver is also used to coat Compact Disks (CDs) and Digital Video Disks (DVDs). In addition, silver is employed in Plasma Display Panels used in television sets and monitors.

3.3.2 Ag^0: catalytic applications

Silver is a unique catalyst for oxygen activation. Some crucial catalytic reactions like the synthesis of ethylene oxide and formaldehyde are run with metallic silver supported catalyst, and more than 700 tons of silver annually are used in the world's chemical industry for the production of two compounds.

Though ethylene epoxidation was first discovered early in 1931 [34] and commercialized in 1938, the mechanism of this reaction is still of great interest for both research and industry. As a heterogeneous catalytic reaction, it involves adsorption, surface reaction and desorption, and a number of adsorbates besides transition state intermediates that are usually very difficult to identify. The electronic structure of metallic silver supported on α-Al_2O_3 catalyst determines how the reaction proceeds is, on the other hand, determined by the property of bulk and surface characteristics of the catalyst. The sizes and morphology of catalyst particles and surface structure (defects of different sizes and dimensions), which are usually on nano/microscale, play decisive roles in the reaction and is affected by impurities and promoters in the catalyst and the procedure for catalyst preparation.

Ethylene may either be selectively oxidized with oxygen over a silver catalyst to form ethylene oxide or totally oxidized with the products carbon dioxide and water. Furthermore, subsequent deep oxidation of ethylene oxide initially formed is possible. The ethylene oxide formation is moderately exothermal (-105 kJ/mol), while the total oxidations of both ethylene and ethylene oxide are strongly exothermal (-1327 and -1223 kJ/mol), so that the reaction must be quenched

to prevent full oxidation [35]. In the conventional industrial process, a total of -350 to -550 kJ/mol are generated, causing hot spots and heat removal problems, which lead to bad selectivities [36].

3.4 Ag^0NP synthesis

3.4.1 Synthesis methods: an overview

There are several methods for creating nanoparticles, each of them bringing some advantages and drawbacks, often linked to the period in which the method was developed first. Some of them are:

- Attrition: macro or micro scale particles are ground in a ball mill, a planetary ball mill, or other size reducing mechanism. The resulting particles are air classified to recover nanoparticles. The diameters of the particles usually cover a wide range of values.
- Pyrolysis: a vaporous precursor (liquid or gas) is forced through an orifice at high pressure and burned. The resulting solid (a version of soot) is air classified to recover oxide particles from by-product gases. Pyrolysis often results in aggregates and agglomerates rather than single primary particles.
- Citrate reduction: introduced in 1951 by Turkevich, it is based on the reduction in an aqueous medium of a source of metallic ions by citrate. Regarding gold it has been refined by Frens allowing the synthesis of NP of pre-chosen size by varying the ratio between the reducing/stabilizing agents. Citrate is the most frequent reductant and stabilizing agent used and gives its name to the method, but a wide range of reductant and stabilizing agents can be used [37; 38] (sugars, organic acids, high-weight polymers, and so on)

- Two-phase synthesis (Brust-Schiffrin): the synthesis is conducted with water and a second medium not miscible with it. Particles are synthesized in water and then transferred to the organic medium. Stabilization with thiols allows them not to irreversibly aggregate or decompose.
- By thermal plasma. The thermal plasma temperatures are in the order of 10,000 K, so that solid powder easily evaporates. Nanoparticles are formed upon quenching (very fast cooling) of the resulting mixture of plasma gas and materials vapors while exiting the plasma region. The main types of the thermal plasma torches used to produce nanoparticles are dc plasma jet, dc arc plasma and radio frequency (RF) induction plasmas. The plasma gas does not come in contact with electrodes, thus eliminating possible sources of contamination and allowing the operation of such plasma torches with a wide range of gases including inert, reducing, oxidizing and other corrosive atmospheres.
- Sol-Gel: the sol-gel process is a wet-chemical technique (also known as chemical solution deposition) widely used recently in the fields of materials science and ceramic engineering. Such methods are used primarily for the fabrication of materials (typically a metal oxide) starting from a chemical solution (sol, short for solution) which acts as the precursor for an integrated network (or gel) of either discrete particles or network polymers [39].

In the case of the colloid, the volume fraction of particles (or particle density) may be so low that a significant amount of fluid may need to be removed initially for the gel-like properties to be recognized. This can be accomplished in any number of ways. The simplest method is to allow time for sedimentation to occur, and then pour off the remaining liquid.

Centrifugation can also be used to accelerate the process of phase separation.

Removal of the remaining liquid (solvent) phase requires a drying process, which is typically accompanied by a significant amount of shrinkage and densification. The rate at which the solvent can be removed is ultimately determined by the distribution of porosity in the gel. The ultimate microstructure of the final component will clearly be strongly influenced by changes implemented during this phase of processing. Afterwards, a thermal treatment, or firing process, is often necessary in order to favor further polycondensation and enhance mechanical properties and structural stability via final sintering, densification and grain growth. One of the distinct advantages of using this methodology as opposed to the more traditional processing techniques is that densification is often achieved at a much lower temperature.

The precursor sol can be either deposited on a substrate to form a film (e.g. by dip-coating or spin-coating), cast into a suitable container with the desired shape (e.g. to obtain a monolithic ceramics, glasses, fibers, membranes, aerogels), or used to synthesize powders (e.g. microspheres, nanospheres). The sol-gel approach is a cheap and low-temperature technique that allows for the fine control of the product's chemical composition. Even small quantities of dopants, such as organic dyes and rare earth metals, can be introduced in the sol and end up uniformly dispersed in the final product [40, 41].

- Sonolysis: an ultrasounds assisted synthesis close to the citrate one.
- Laser ablation: a laser ablates nanosized fragment of metal from a bulk matrix

4. Low-organics synthesis of silver nanoparticles: method, characterization and applications

4.1 Our synthetic approach

For synthesizing our sample we decided to work on the citrate route revisiting classical Turkevich method. In fact our aim was to produce nanoparticles (NP) without relying on high-molecular-weight compounds to complex them and to protect them against coalescence phenomena. In fact, they represent a catalytic issue since removing these protecting compounds in order to obtain supported “naked” nano-sized metal catalysts can be a difficult goal to achieve.

Our main points during the development and the study of feasibility of this synthesis have been:
1) using an as-low-as-possible amount of reductants
2) avoiding high-molecular-weight stabilizers
3) working with an aqueous medium (for a greener, safer and more sustainable approach)

Six colloidal solutions were prepared following a modified Turkevich method [42]. $AgNO_3$ aqueous solution was heated to boiling and organic reductants were added to a certain reductant / Ag molar ratio.
Silver nitrate (99.98%) citric acid (99%), ascorbic acid (99%) and NaOH were purchased from Sigma Aldrich. All the reagents were of analytical grade and were used without further purification.
As mild organic stabilizers/reductants solutions of trisodium citrate were used. For some synthesis a

small amount of disodium ascorbate was added in order to tune the reducing power.
All solutions were freshly prepared for every synthesis.
We tested two different concentrations of Ag^+ ions (0.3 mM and 1.0 mM) and correspondingly two different quantities of reductant. were tested.

All solutions became coloured in few minutes after the addition of the reductant, ranging from a dark green/ brown-red color to a gold/ochre one. After the change of color, the solutions were kept boiling for 30 min. All solutions were then centrifuged (4000 rpm, 30 min) in order to separate the grayish suspension of Ag^0 formed during the synthesis. In order to explore different ways to control size, shape and time of synthesis we repeated the two synthesis with an higher content of reductant at a temperature of 283 K.
In that case we kept the colloidal solution at 283 K under stirring for 30 min after the change of color.
See table 2 for a quick overview of different synthesis:

Table 2

Synthesis	[Ag+] (mM)	Citrate / Ag+ (mol/mol)	ascorbate / Ag+ (mol/mol)	T (K)
a	0.30	2.00	0.00	373
b	0.30	2.00	0.30	373
c	1.00	7.50	0.00	373
c	1.00	7.50	2.00	373
e	1.00	7.50	0.00	283
f	1.00	7.50	2.00	283

4.2 Ag^0NP characterization

4.2.1 UV.VIS spectroscopy

UV-Vis spectra are a common, quick and cheap method of characterization of colloidal solution of metal nanoparticles thanks to the surface Plasmon resonance band often showed in the visible by this materials.

UV-VIS absorption spectra were recorded on a Perkin Elmer, in a 1 cm optical path cuvette, with a data interval equal to 1nm and a Scan speed of 120 nm/min.

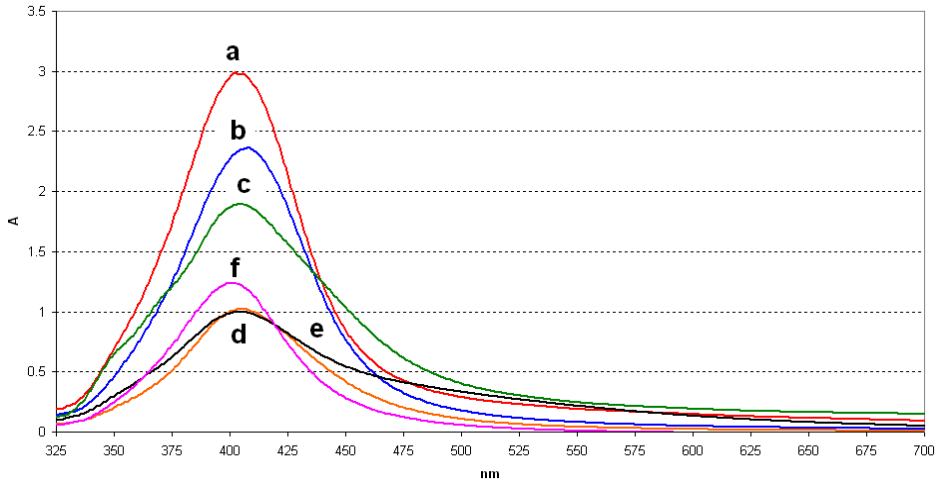

Fig. 17 UV-VIS spectra of colloidal solutions after synthesis.

Figure 17 shows the UV-VIS spectra of the Silver colloid in the range 325 nm – 700 nm. The absorption band in visible light region (350 nm – 550 nm, plasmon peak at around 400 nm) is typical for spherical silver

nanoparticles [43]. The plasmon peak position and the FWHM depend on particle mean diameter and on the extent of colloid aggregation [44].

To monitor the stability of silver colloids, we measured the absorption of the colloid over time for months. Colloidal solutions were stored at room temperature, without exposing them to light. The evolution of UV-VIS spectra is shown in Figure 18. we present only the three samples we studied for more time, since other samples haven't been followed for enough time to result significant.

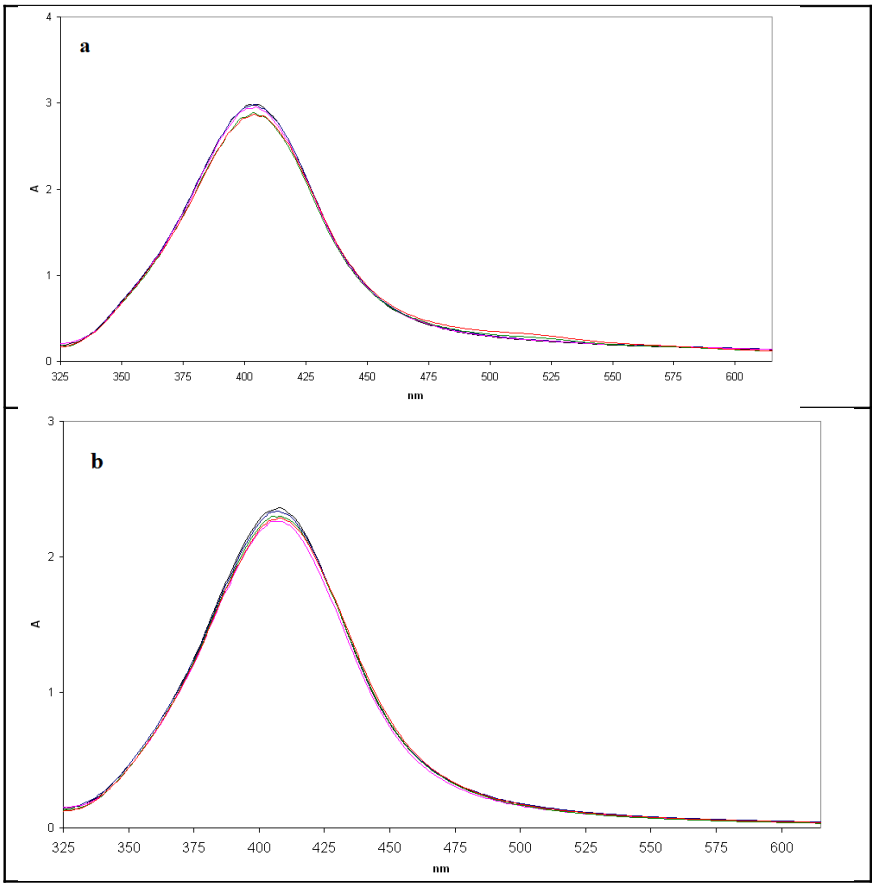

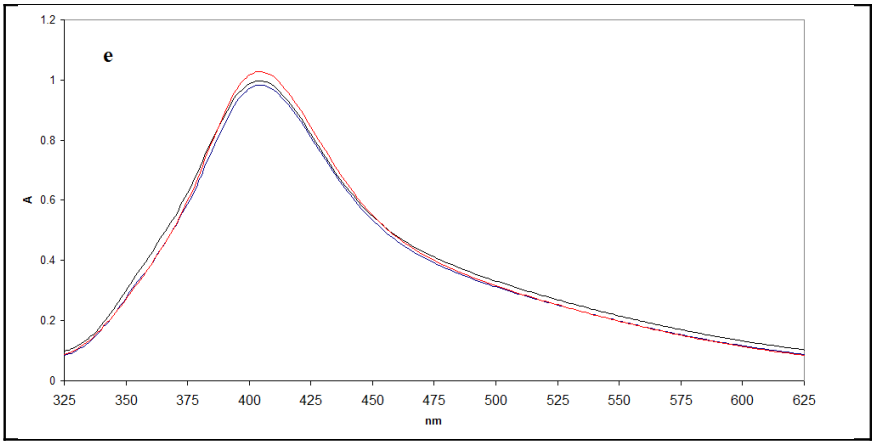

Fig. 18 spectra of the ageing of sample a), b) and e)

There were no obvious changes in absorbance and peak position for three months. As the particles increase in size, the absorption peak usually shifts toward the red wavelengths [45]. Increase of absorption indicates that amount of silver nanoparticles increases. An unchanged peak position indicates that particles don't undergo aggregation or coalescence phenomena, thus confirming the stabilization power of citrate.
An unchanged absorption maximum indicates an absence of nucleation and growth after-synthesis phenomena, thus leading to a stable and predictable material.

4.2.2 SEM characterization

Scanning Electron Microscopy (SEM) is a valuable tool to make a first size and shape evaluation of nanoparticles. Even though TEM is the most suitable technique for this purpose, unfortunately Transmission Electron Spectrometers are not as common as SEM and required long time for analysis and very well

trained operator. Therefore, as stated above, we conducted basic analysis on our sample by the means of SEM facility at SMETEC, University of Bologna

Sample for SEM examinations were prepared by filtering a small amount of the colloidal solution on Anodisk™ membranes with a pore size of 20 nm. SEM micrographies of Anodisk™ membranes loaded with AgNP were taken with a EVO ZEISS microscope, with a magnification of 200.00 X and an EHT of 25 kV.

In order to limit filtering-related aggregation phenomena, after sample a and b preparation we reduced the quantity filtered thus obtaining a better dispersion.

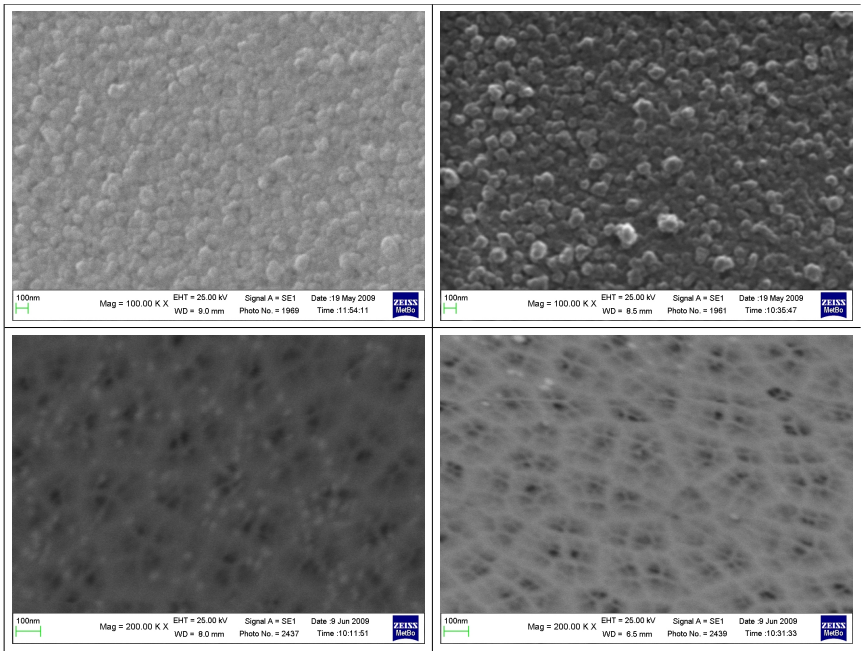

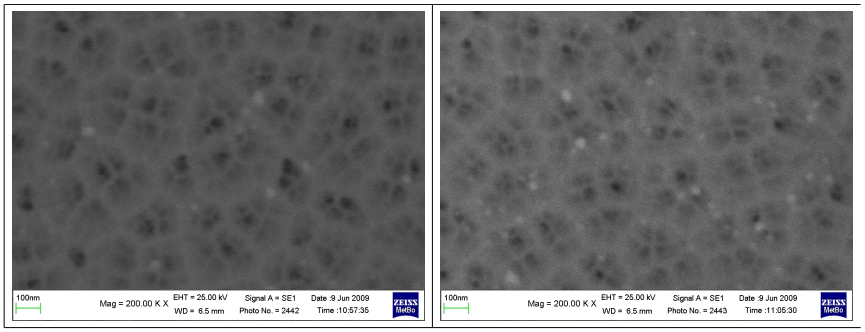

Fig. 19 first row, from left to right: SEM pictures of samples 01), 02), second row, from left to right: SEM pictures of samples 03, 04), last row, from left to right: SEM pictures of samples 05), 06);

SEM micrographies show pseudospherical NP with a mean diameter of 50 nm for synthesis 01 and 02 and around 20 nm for synthesis 03 and 04.
Low temperature synthesis 05 end 06 shows a wider dispersion in diameters, ranging from 20 to 50 nm.

4.2.3 TEM characterization

During my internship period spent at the Heyrovsky Institute in Prague we could take some TEM picture of one of our samples.

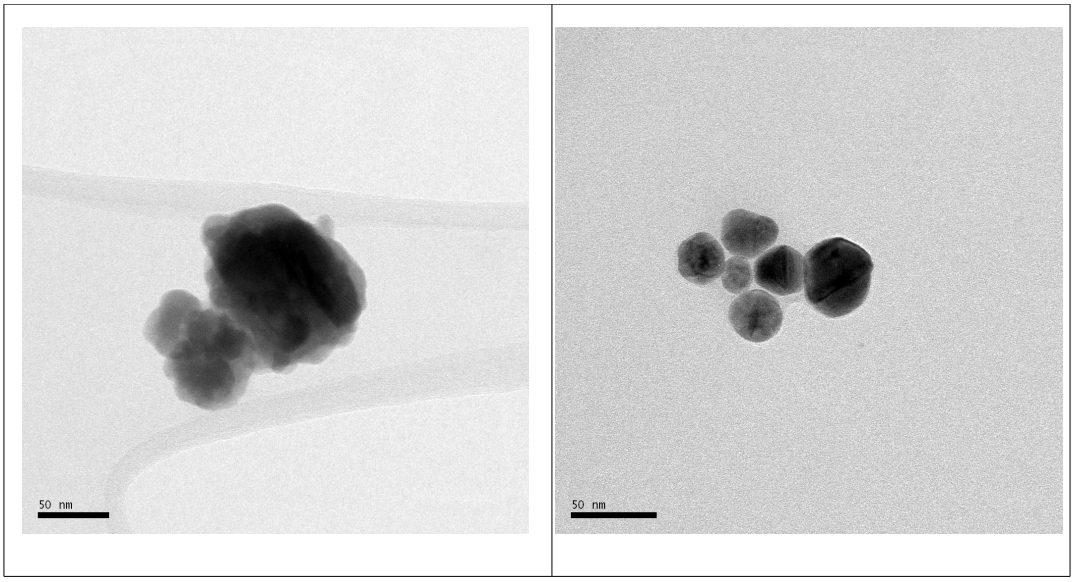

Fig. 20 TEM pictures of sample 02

TEM pictures allowed us to elucidate that nanoparticles with diameter around 50 nm seen by SEM were actually made up by aggregation of smaller nanoparticles with diameter around 10 nm. Citrate can play a good stabilizing role in medium range interactions, preventing formation of microparticles rather than nano- ones during and after the synthesis, but at the molar ratio we used it lacks capability of stabilizing particles during the first stages of growth.

4.3 Development of a yield calculation method

Since after every synthesis some Ag^0 went lost in the centrifugation we developed a method to quantify the yield in colloidal silver (fig. 21).

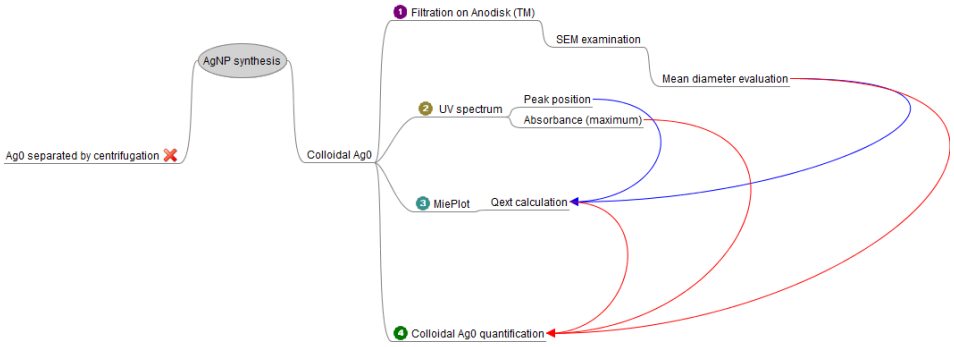

Fig. 21: Mind map of the yield calculation method applied to our synthesis

We used the free software MiePlot [46] to calculate the single Ag^0NP Qext in a water medium, then we calculated the number density of particles and finally the weight of Ag^0 in colloidal form available in solution [47].
Step 1 (mean diameter evaluation by SEM) may be skipped if synthesis are routinely performed with a well established method and a calibration has been made between UV spectra and mean diameter obtained. In this case, this quantification method becomes an attractive alternative to TEM analysis as “quality control” routine.

Results are summarized in table 3:

Table 3: yield calculated for our synthesis

Synthesis	Yield %
A	52
B	36
C	57
D	28

We can see that citrate-only synthesis lead to better yields, thanks to the milder reducing power of citrate, while synthesis conducted with a small amount of ascorbate in addition show lower yields in AgNP probably due to a reduction rate too fast and not matched by stabilization rate by citrate.

4.4 ELETTRA

We had the possibility to access ESCAMicroscopy beamline at ELETTRA synchrotron facility in Trieste, Italy to run some tests on our nanoparticles, exposing them to different reactive gases and temperatures.

Our sample 03 has been concentrated about 100 times by several filtrations on Anodisk™ membranes (20 nm) Then at the beamline this concentrated sample has been manually deposited on Si plates dropping a small amount of colloid on each of them

4.4.1. ESCAMicroscopy

The Si-Ag^0NP sample has then been checked by SEM-EDX to verify if Ag^0 is enough to run some tests and to check if there are some contaminants.

We detected the organics used during the synthesis and in order to guarantee the full accessibility to the reactant gases the sample has been put in place in the beamline sample holder and them sputtered with Ar^+ ions (1 kV for 20 minutes).

After the sputtering no significant traces of C were detected.

Unfortunately it was not possible to check the presence of Na^+ ions since XPS signals overlap with the Ag^0 ones.

Beamline scientists optimized all the instrumental parameters required for spectra registration

The examined XSP spectrum zones were

- survey (100 - 654 eV)
- Ag (275 - 290 eV)
- O 1s (114 - 130 eV)
- C 1s (362 - 376 eV)
- Si (544 - 558KeV)
- Valence Band (647 - 655 eV)

The beam is highly reductant and modifies the illuminated zone in a short time. All tests have to run time by time on different zones for this reason.

Every time we tried to choose zones that were similar the ones previously examined.

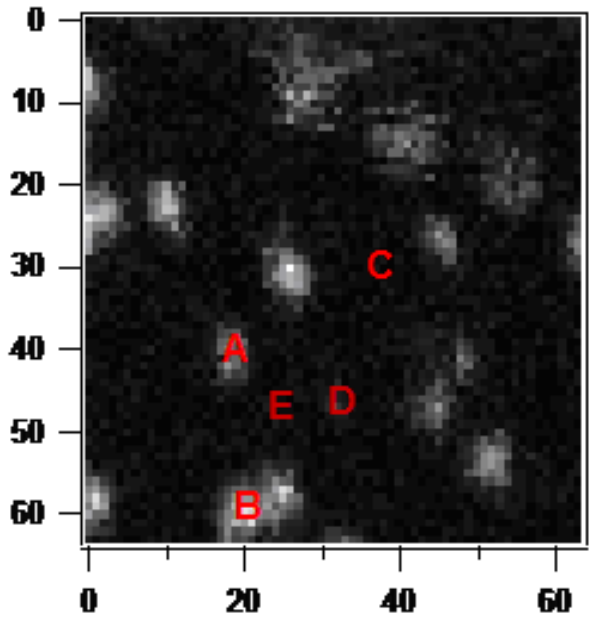

Fig. 22: A-E zones Ag-chemical map

A: medium size particles aggregate
B: bulk aggregate
C: flat (Si plate, Ag not detected)
D: faint particle, very low Ag concentration
E: flat (Si plate, Ag not detected)

4.4.1.1 Silver spectra features

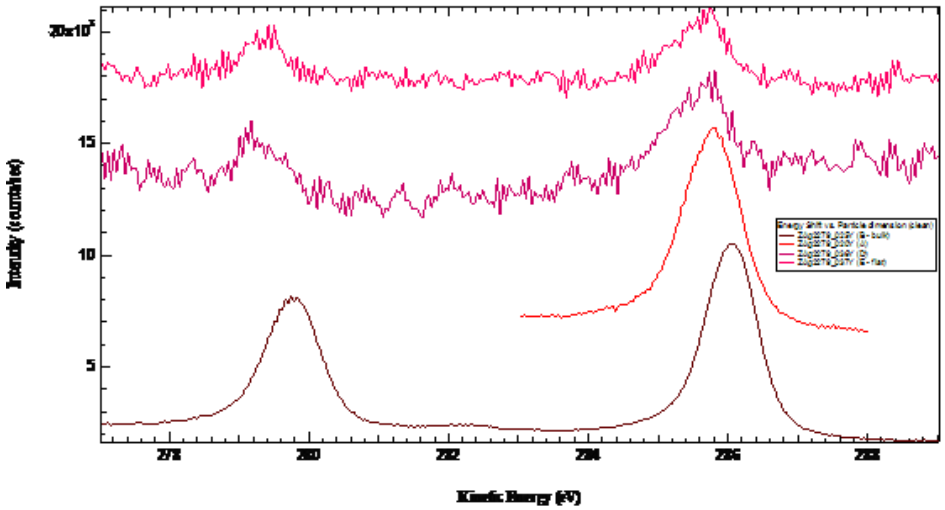

Fig. 23: Ag spectra for A-E zones

For this very first set of points we didn't record spectra for C.

Different zones have Ag XPS spectra with a very similar pattern. It is useful to note that Ag characteristic bands are shifted (and in some case with an higher FWMH) depending on the examined zone

A band shift towards higher keV is related to a lower electron binding energy, referable to an electronic state that differs from the reference one.

About our samples, we can't exclude that such shift was linked to a different number of nanoparticles under the beam, therefore to different aggregation degrees in the examined zones.

4.4.1.2 O_2 10^{-6} mbar, 50°C, A-D

After the first spectra taken at room temperature and in an inert environment the sample was exposed to an oxidant atmosphere (10^{-6} mbar O_2) and heated up to 50°C.

Overnight we recorded oxygen spectra for points A-D

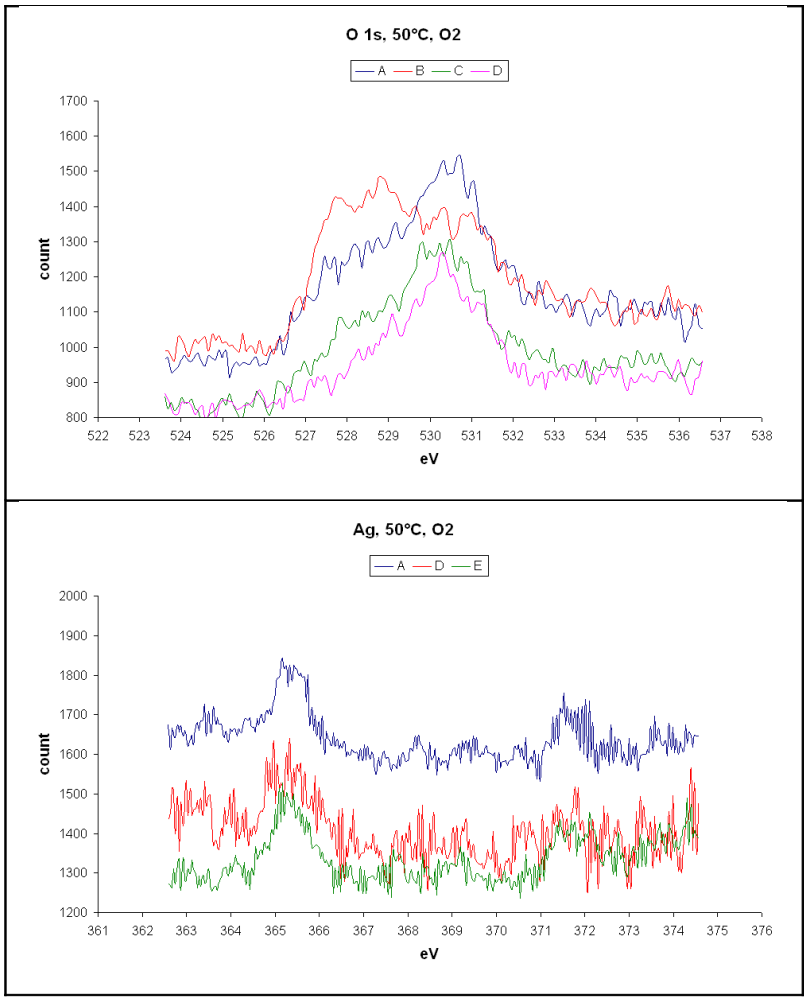

Fig. 24: O 1s and Ag spectra for A,D,E zones after oxidation at 50°C

We also recorded Ag spectra but the chemical contrast was getting lower and lower due to a damaging of the zone.

This damaging is referable to the formation of a layer of coke from C-containing molecule present in the sample holder chamber due to irradiation of the beam.

4.4.1.3 O_2 10^{-6} mbar, 50°C, 6 hours oxidation, F-I

We chose a new zone, identifying the following particles:

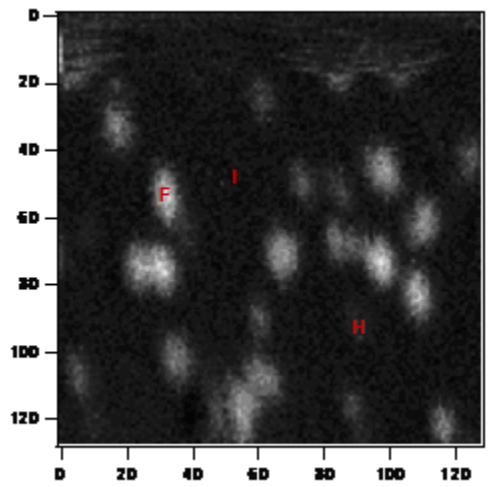

F: medium aggregate

G: letter skipper buy the operator

H: *faint* particle, very low Ag concentration

I: *flat* (Si plate, Ag not detected)

Fig. 25: F, H, I zones Ag-chemical map

We took again the same array of spectra.

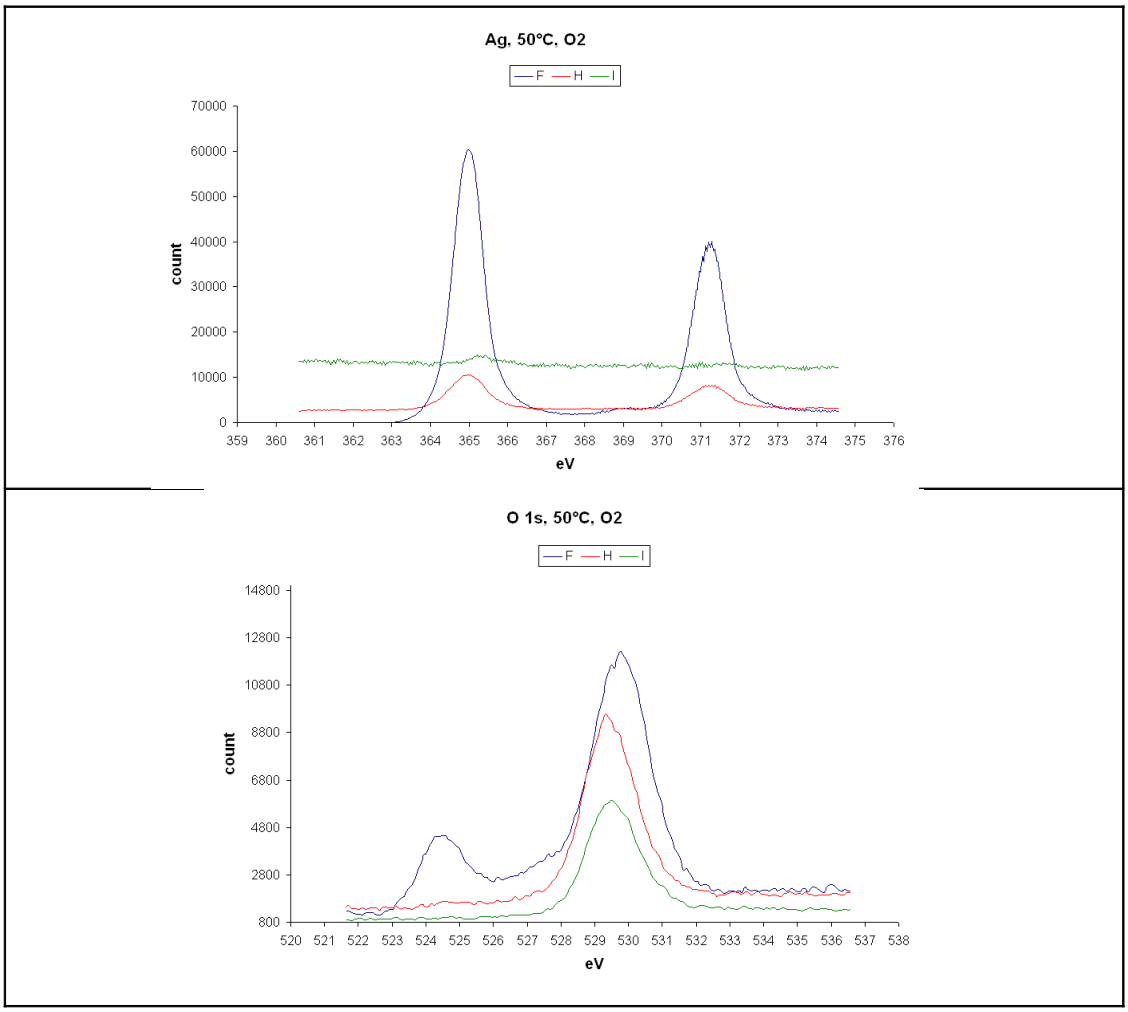

Fig. 26: O 1s and Ag spectra for F, H, I zones after oxidation at 50°C

We can underline that Ag bands maxima are shifted as above and that in oxygen spectra taken on bigger aggregates there's a second spectral component at higher eV, therefore related to species with a lower binding energy.

At this time we and the beamline scientists haven't been able to give an attribution to this band, since it present values totally unexpected in an oxygen spectrum.

We run more tests to confirm this second oxygen band for bulky particles. We chose an L zone, comparable with A and F, and after 6 hours of exposition to a partial pressure of 10^{-6} mbar of O_2. At 50°C we obtained these spectra:

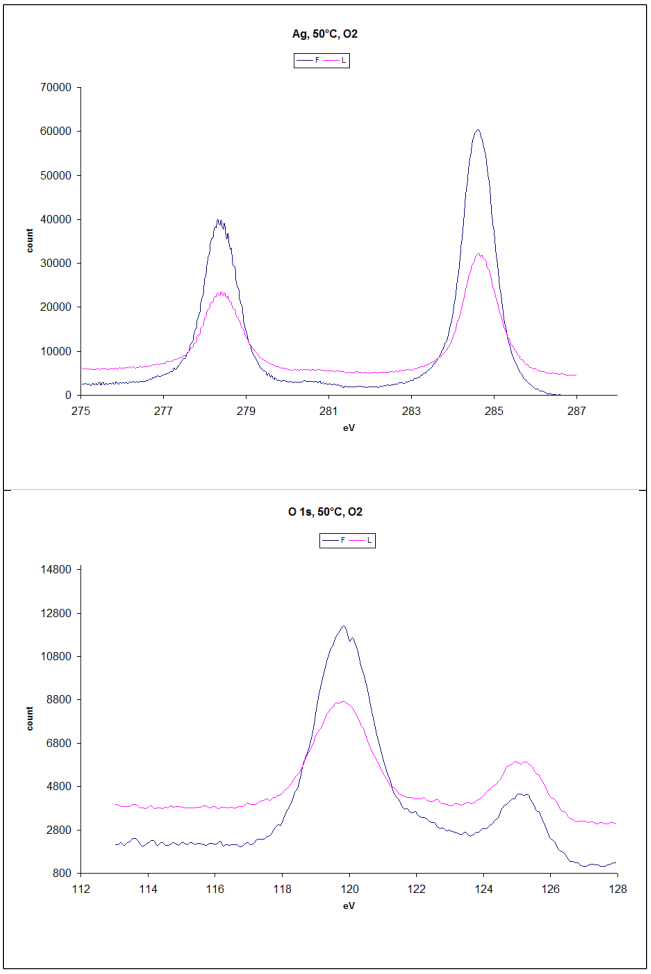

Fig. 27: O 1s and Ag spectra for F, L zones after oxidation at 50°C

Apart from different signal intensities related to a different quantity of silver in the irradiated zone, silver bands are almost the same.

Oxygen spectra confirm the presence of a second component, not detectable in zones with a low concentration of silver.

After this cycle of analysis also the L zone were fatally compromised by the irradiation beam.

4.4.1.4 Ag-O interactions on extremely large aggregates

We examined an extremely wide particles aggregate (M).

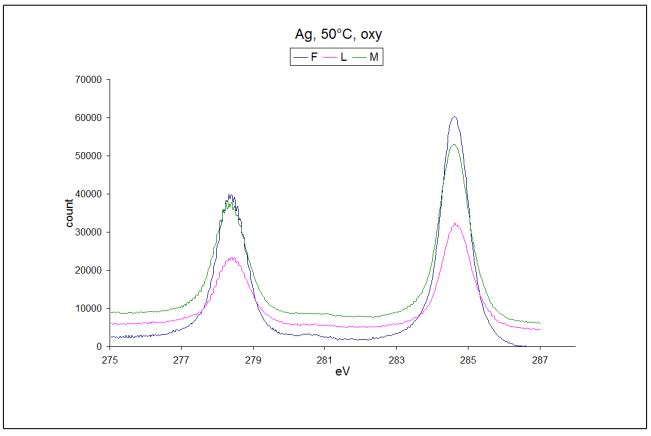

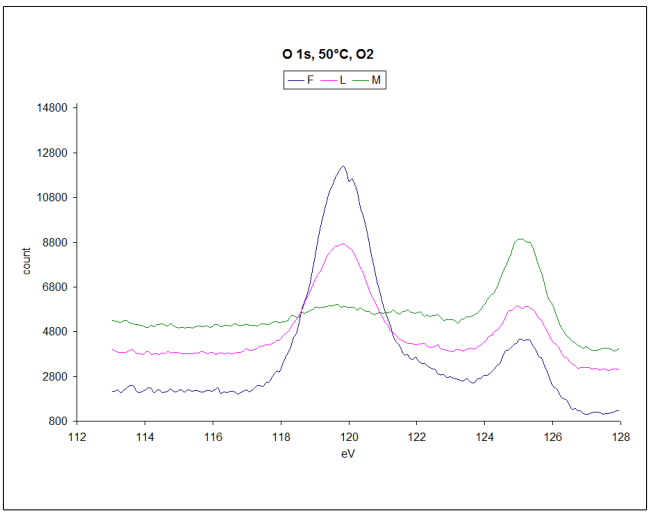

Fig. 28: O 1s and Ag spectra for F, L,M zones after oxidation at 50°C

We could further confirm the second "unusual" component fin oxygen spectra. In this case it is even predominant.

We characterized the M zone also at room temperature:

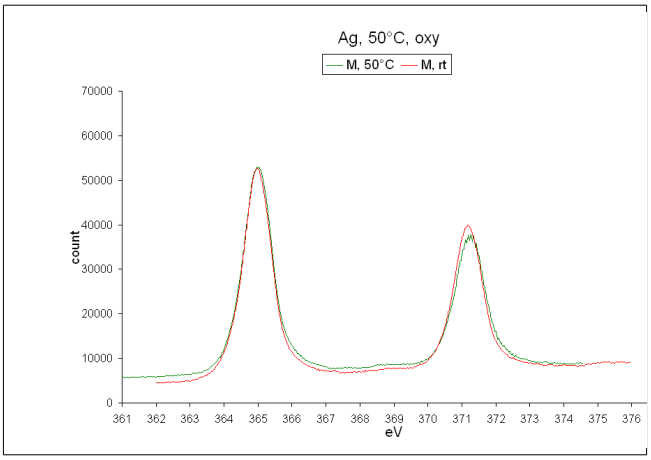

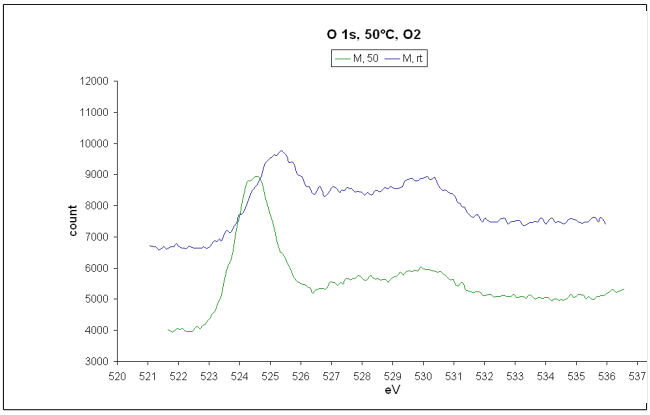

Fig. 29: O 1s and Ag spectra for M zones after oxidation at 50°C and at RT

O 1s bands show now different relative intensities and a shift for the component at lower BE.

Beamline scientists related this to the possibility that irradiating an aggregated zone of some micrometers the beam and/or the change of temperature could have modified the sample or shifted the beam focus

4.4.1.5 H_2 10^{-6} mbar, RT

We dosed H_2 (10^{-6} mbar) at room temperature for 20 minutes.

O 1s spectra recorded on M zone showed very low quality. A quick survey revealed a C layer that made the whole zone no more suitable for spectra registration. Also checking other zones all surveys shows very high C signals after few minutes of irradiation. Such a quick fouling of the sample didn't allow meaningful spectra recording.

Sample were left under H_2 (10^{-6} mbar) at 50°C for 90 minutes.

After higher temperature reduction the beam seems to have the opposite effect, diminishing the carbon presence during irradiation.

We chose a bulky agglomerate (N) with a less dense zone close to it (O).

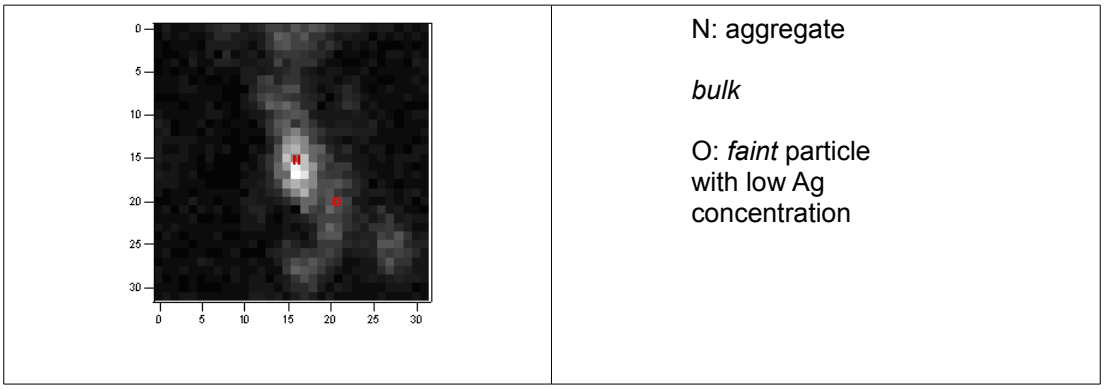

Fig. 30: N, O zones Ag-chemical map

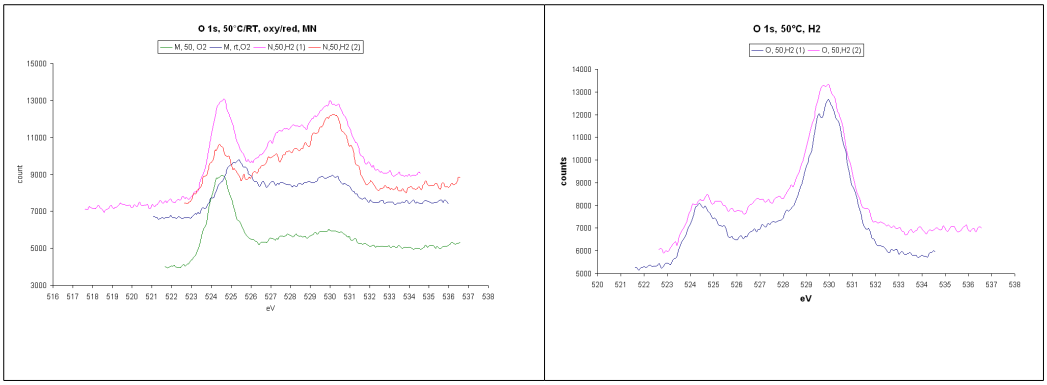

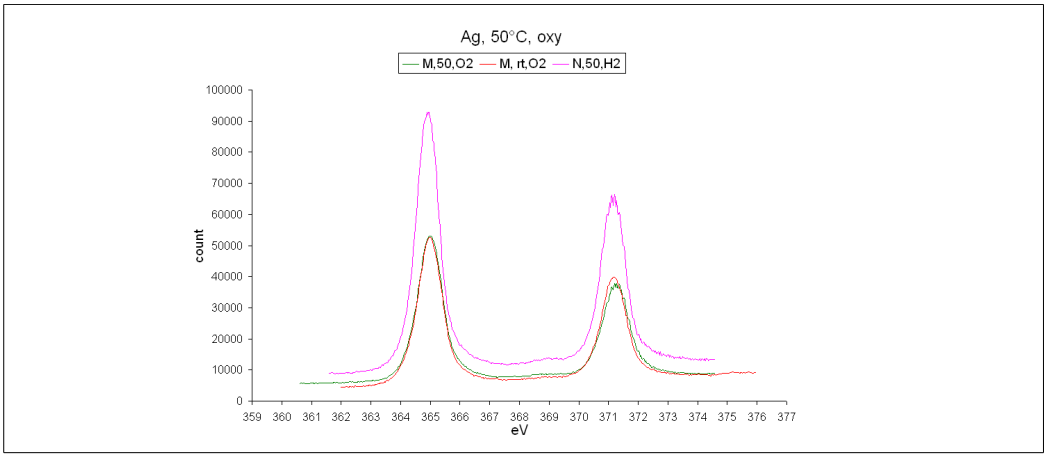

Fig. 31: O 1s and Ag spectra for M, N, O zones after reduction/oxidation treatments at 50°C and at RT

Having elucidated that

- Synchrotron beam is highly reductant
- A full array of spectra (survey, Ag, O, C, Si, VB) requie about 30 min

We decided to start each array of spectra with a O 1s spectrum recording and then concluding the analysis recording another O 1s spectrum after the others.

In O1s spectra for N it's now possible to find even three components. The central one, just a shoulder in spectra of similar particles, is now evident.

We would like to underline that after the staying of the beam on the O zone this appeared more "bright" and similar to N, showing a larger quantity of detectable Ag than before.

4.4.1.6 - H_2 10^{-6} mbar, 50°C – P-S

Since we didn't encounter any amore graphitization phenomena we characterized a new set of particles (bulk, flat, faint) to check hydrogen effect after an oxidation treatment.

As above, spectra were taken starting with O 1s and after the whole array another O 1s spectrum is recorded to check differences.

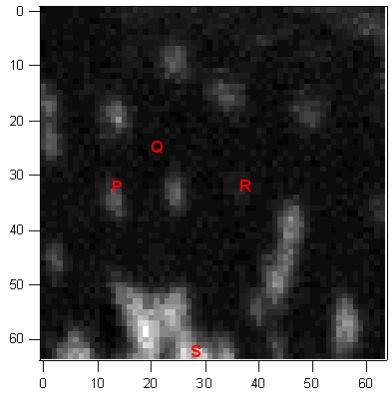

P: *bulk aggregate*

Q: *flat* (Si plate, Ag not detected)

R *faint* particle, very low Ag concentration

S:large bulk aggregate (similar to M)

Fig. 32: P-S zones Ag-chemical map

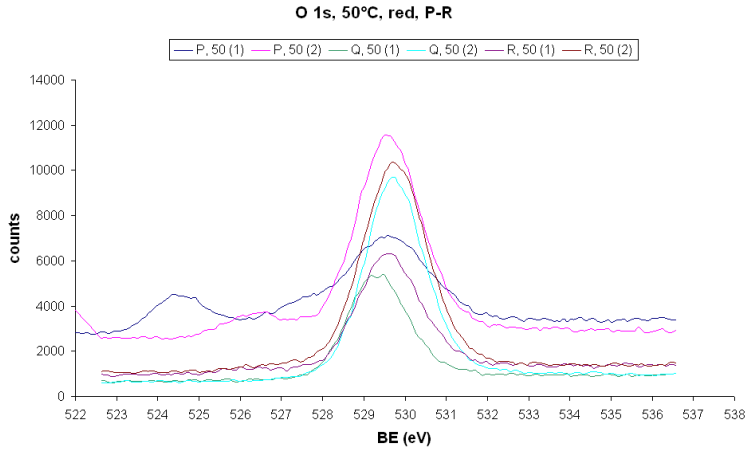

Fig. 33: O 1s spectra of P, Q, R zones after reduction at 50 °C

It is clear that during the 30 minutes required to record the array of spectra O 1s bands are noteworthy modified. The second, "new" component of O 1s spectra of P particle has a lower intensity and is shifted toward higher BE.

The main O 1s band presents a different shift for particle Q (+0.3 eV) and P (-0.08 eV). This could be due to a different convolution of the two component, while it remains unchanged for S particle.

4.4.1.7 - O_2 10^{-6} mbar, 100°C – P-S

Sample was kept under H_2 at 100°C overnight to remove from the surface any traces of oxygen in order to start another oxidation cycle followed by feeding ethylene.

Zones P-R are checked again

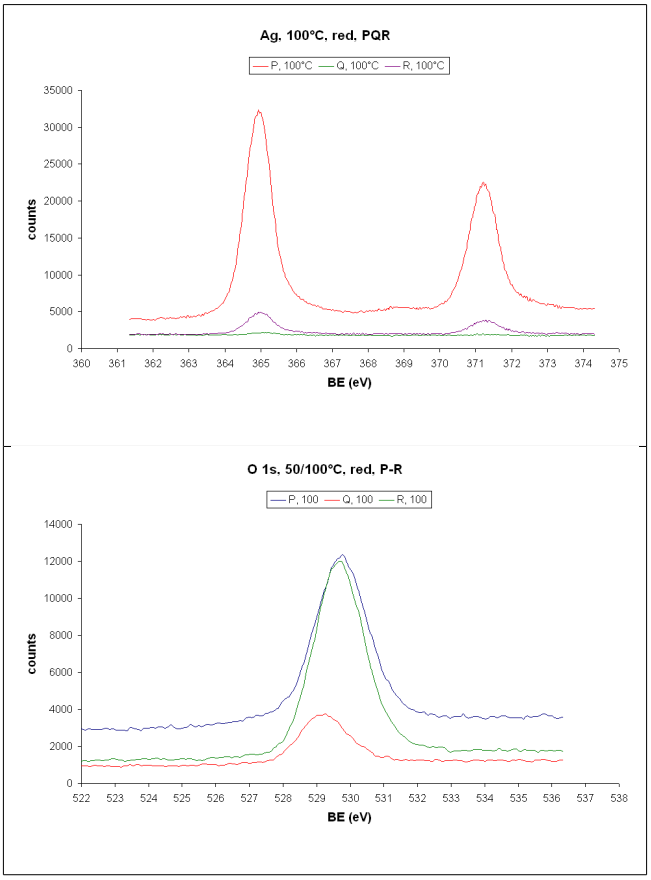

Fig. 34: Ag and O 1s spectra of P, Q, R zones after reduction at 50 °C and 100 °C

The unidentified component in O1s disappeared.

We started a new oxidation cycle (O_2 10^{-6} mbar, 100°C)

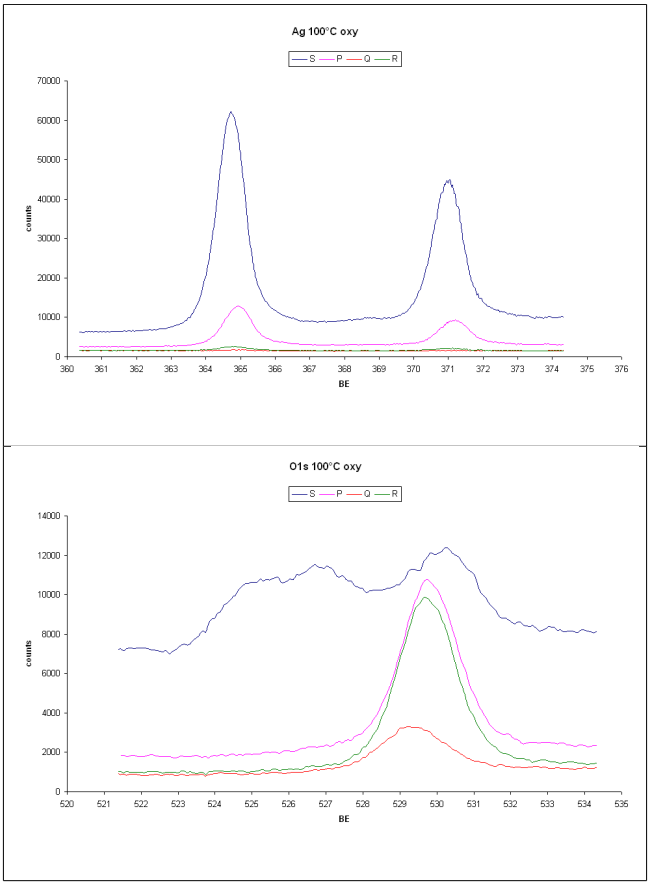

Fig. 35: Ag and O 1s spectra of P, Q, R, S zones after reoxidation at 100 °C

At the beginning no changes were observed in O 1s bands. After 90 minutes of exposition at 100°C some changes started to take place.

In bulk particles as P the second band didn't' appear again, while on very large aggregates like S it appeared again with an intensity comparable to the one of the main band, but it is well visible also the third (middle) component seen on N (an aggregate comparable to S)

4.4.1.8 Ethylene 10^{-6} mbar, 100 °C, P-S

At the end of this set of exploratory tests we fed ethylene on the oxidized sample.

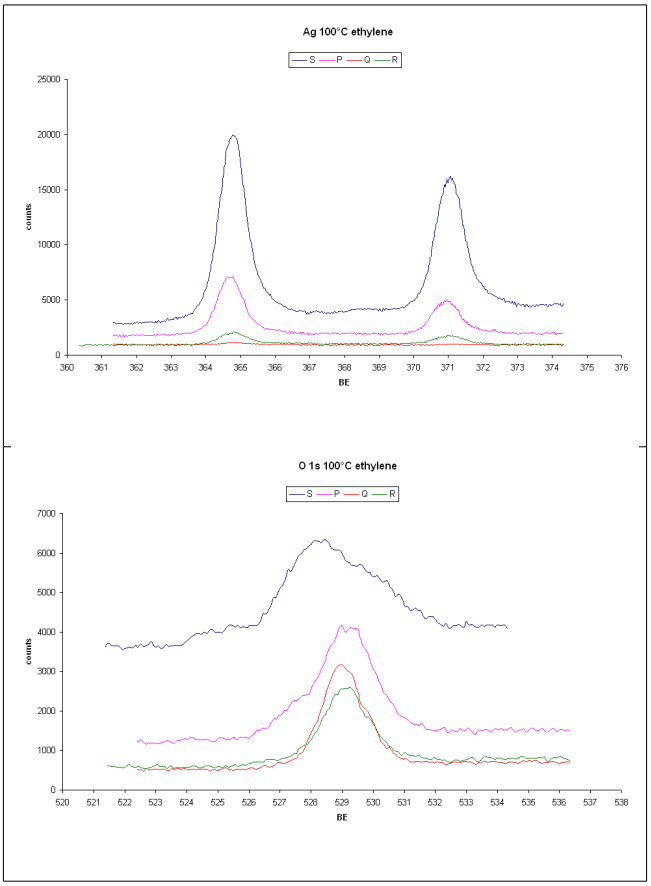

Fig. 36: Ag and O 1s spectra of P, Q, R, S zones after ethylene pulse at 100 °

This pulse caused a shift of almost -1 eV for all the particles.

In particular the O 1s spectrum of S aggregate got totally reconstructed. Bands are more convoluted, maxima are shifted and bands at lower BE almost disappeared.

Ethylene gives rise to interaction phenomena with surface oxygen species. The anomalous band found on larger aggregates showed to be the more reactive

4.4.2. FEG-SEM

At ELETTRA facilities we could characterize our sample deposited on Si plates by Field Emission SEM.

The main difference with respect to SEM is that A field-emission cathode in the electron gun of a scanning electron microscope provides narrower probing beams at low as well as high electron energy, resulting in both improved spatial resolution and minimized sample charging and damage.

Particles are pseudo spherical and partially they follow the orientation of crystalline planes.

Particles show a tendency to aggregate in pseudo spheres with a diameter of microns and a cauliflower-like structure.

Single particles often show on their surface smaller particles (their mean diameter is around 5 nm). These “specifically-nano” particles can also be found well dispersed on Si plate

We can conclude that all the types of aggregates examined are made up by nanoparticles with a mean diameter of 20 nm with different degrees of aggregation, while the faint zones in any case possess

Ag^0 in a well defined form, i.e. 5 nm diameter nanoparticles with no phenomena of aggregation

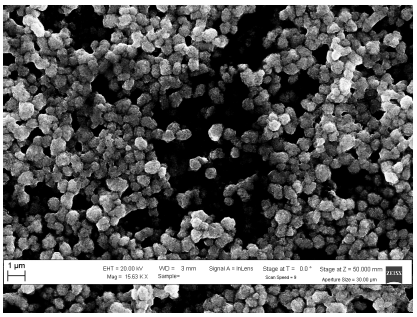

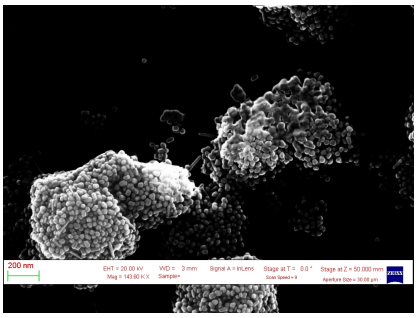

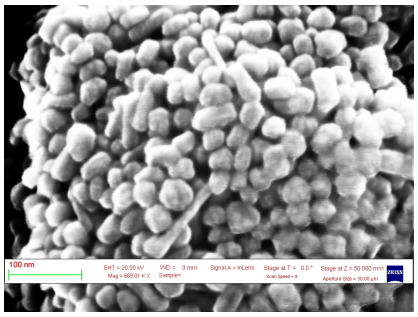

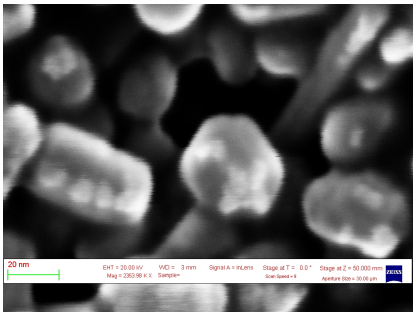

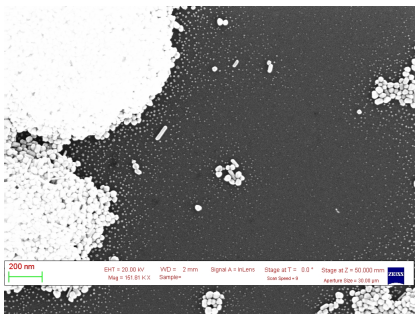

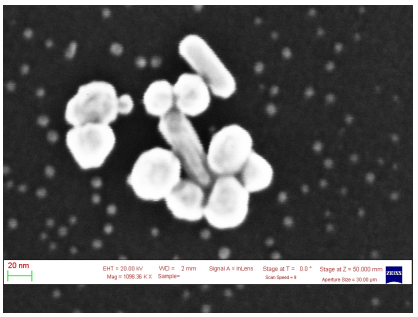

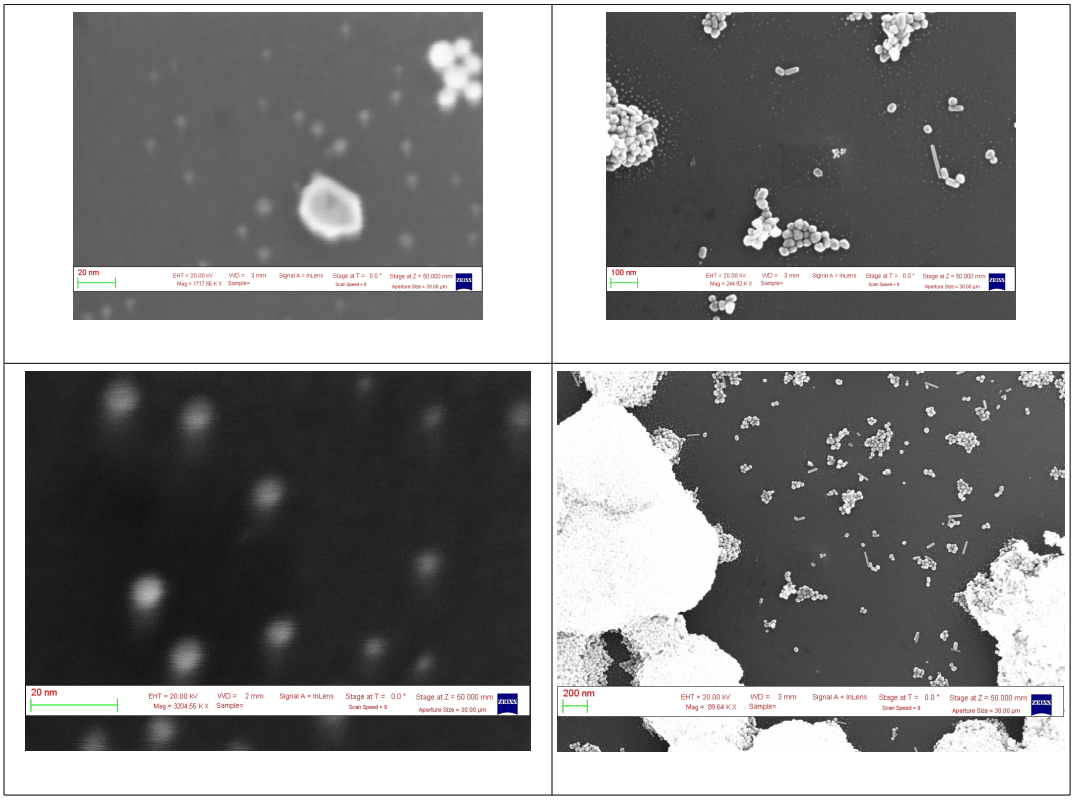

Fig. 37 FEG-SEM micrographies of sample Si-Ag^{0}NP

4.5 Ag^{0}NP as a catalyst for soot decomposition

4.5.1 Diesel environmental concerns

In the last years the polluting particulate matter (PM) emitted by Diesel engines has been drew more and more attention. Because of its negative effects on human health the laws about its levels have been getting more and more tight.

As a consequence a lot of technologies for reducing emissions have been developed. Among them, the filtration followed by catalytic oxidation seems to be promising.

A catalyst allows to bring the soot combustion temperature down to the temperatures of exhaust gases.

CeO_2 is a suitable support for catalysts that have to be used in these reactions since it shows a lot of available surface oxygens and an high surface reducibility.

4.5.2 Catalytic tests for soot decomposition reaction

In collaboration with University of Udine (Italy) we tested supported Ag^0NP (5%) on reducible and non-reducible oxides like ZrO_2 e Al_2O_3.

Samples have been confronted with references synthesized by incipient wetness impregnation starting from $AgNO_3$.

All the samples were calcined in air at 500 °C for 3h (fresh samples) and at 750 °C for 12h (aged samples).

Results are shown in table 4

Sample	T50 (°C)		SA (m^2/g)	
	fresh	aged	fresh	aged
Ce5Ag IW	334	371	37	13
Zr5Ag IW	333	341	45	19
Al5Ag IW	346	355	165	157
Al5Ag	419	447	116	106

After thermal treatments XRD showed the presence of metallic silver. HRTEM measurements confirmed metallic Silver on both aged and fresh samples based on zirconia and allumina (figura 1C e 1D).

Ceria based systems showed a different behaviour. Silver is present both as Ag^0 and as Ag_2O. Ag_2O is in contact with

CeO_2 while metallic Ag is most of the times found on Ag_2O particles (figure 1A).

During calcinations the transformation from Ag_2O to Ag^0 id retarded when in presence of CeO_2 thanks to the strong interactions with this support. It has been possible to elucidate that the decomposition of silver oxide to metallic silver takes place on the opposite side with respect to the CeO_2 side.

In aged samples particles with core-shell structures are formed. On CeO_2 we detected Ag_2O particles covered by metallic silver (fig. 38).

Figura 1: HRTEM Ce5Ag: A, fresh; B, aged
Al5Ag: C, fresh; D, aged

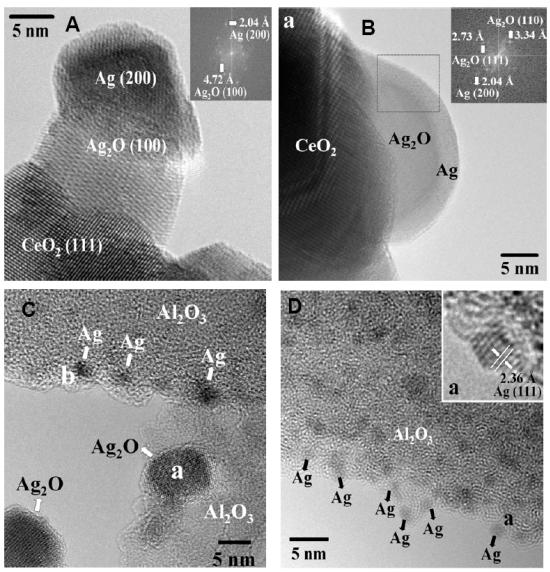

Fig. 38: HR-TEM of Ce5Ag and Al5Ag samples

Ag_2O presence is confirmed also by TPR measurements that show a reduction peak at 120 °C associated to the reduction of the oxide (fig. 39).

This peak is not shown in sample supported on zirconia and allumina.

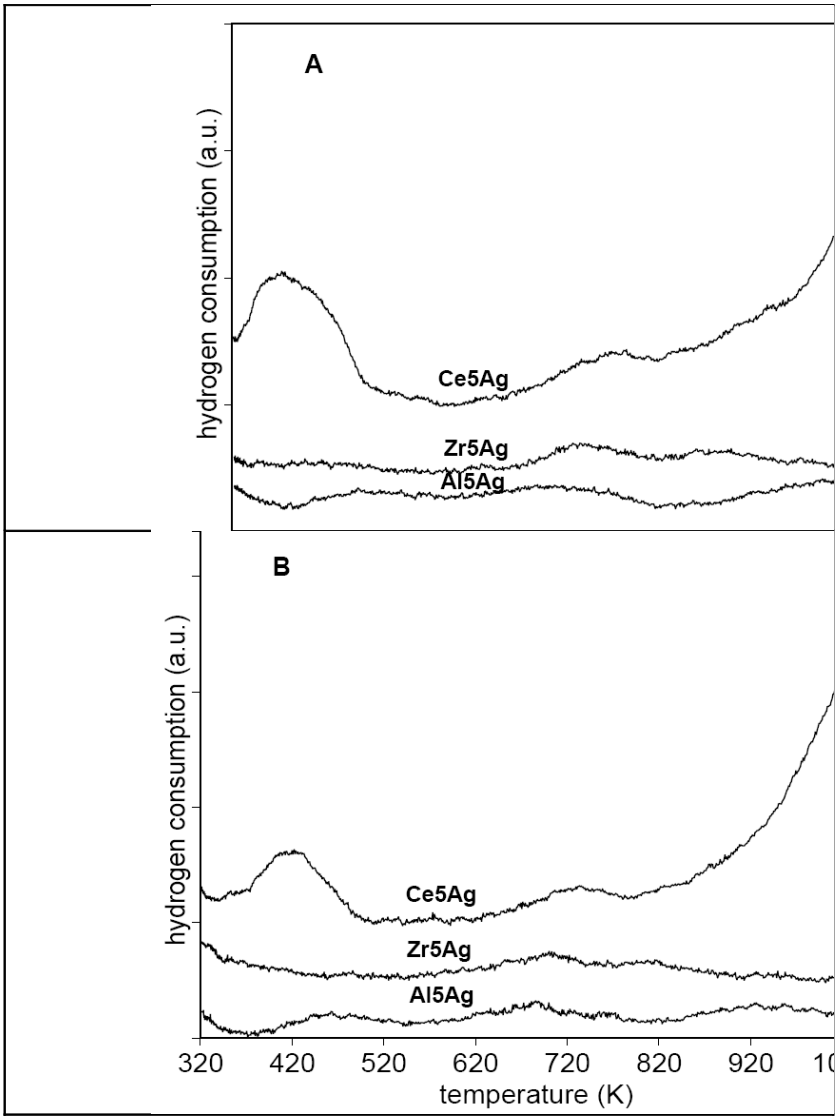

Fig. 39: TPR of fresh samples (A) and calcined ones (B)

Catalytic activities have been tested by thermogravimetric experiments.
Catalysts were mixed in a 20:1 with (Printex U, Degussa soot in tight contact mode (10 minutes in an agate mortar) in order to obtain a good reproducibility (± 5 °C).

T50 parameter, temperature in which we can observe a 50% weight lose, is the value we chose to evacuate the catalytic activity.
The less is T50, the more active is the catalyst.

Sample	T50 (°C)		SA (m^2/g)	
	fresh	aged	fresh	aged
Ce5Ag IW	334	371	37	13
Zr5Ag IW	333	341	45	19
Al5Ag IW	346	355	165	157
Al5Ag	419	447	116	106

Reactivity of supports

Sample	T50 (°C)		SA (m^2/g)	
	fresh	aged	fresh	aged
CeO_2	387	411	49	22
ZrO_2	502	527	59	27
Al_2O_3	611	613	180	159

Reference systems resulted particularly active but while zirconia and alumina based systems didn't show deactivation after the calcination, ceria based system lost their activity after calcinations at 750 °C
Catalytic activity can be related to the formation of non stechiometric surface oxides

Nanoparticles supported catalysts didn't show the same reactivity than the references.
Sample prepared by incipient wetness impregnation both fresh and aged showed better results.

These negative results could be related to a bigger particle size of nanoparticles with respect of reference samples.

XRD of fresh sample show metallic silver and peaks of nanoparticle-based sample are more intense than the reference samples ones (fig. 40).
In the aged sample we can observe a netta diminuzione of metallic Silver peaks and the formation of a $AgAlO_2$ phase.

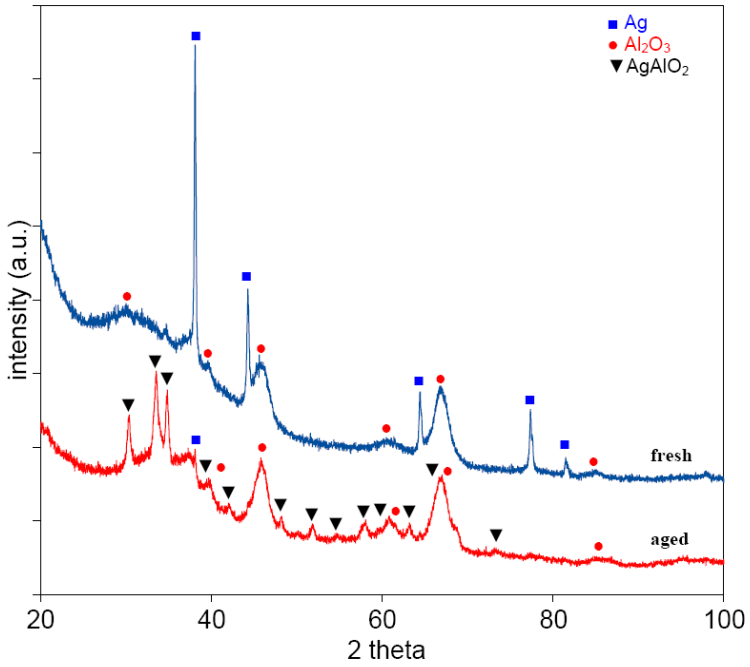

Fig. 40: XRD pattern of Al5Ag sample after catalytic tests

The formation of this phase probably causes a further decrease of the activity.

5. References

[1] Herreros B., *The X-Ray Diffraction Zeolite Database* (http://suzy.unl.edu/bruno/zeodat/zeodat.html)
[2] Meier W. M. et. al., *The Atlas of Zeolite Structure Types* (http://www-iza-sc.csb.yale.edu/IZA-SC/Atlas/AtlasHome.html)
[3] Subhash B., *Zeolite Catalysis: Principles and Applications*, CRC Press, Inc., Boca Raton, Florida, 1990.
[4] Nishi K., Thompson R., *Handbook of porous materials*, Chapter 4.2.2. Synthesis of Classical Zeolites, 2008
[5] Revista Facultad de Ingenieria, Issue 53, June 2010, Pages 30-41
[6] Applied Clay Science, Volume 42, Issue 3-4, January 2009, Pages 446-454
[7] Tavolaro A. et al., Advanced Materials, Volume 11, Issue 12, 1999, Pages 975-996
[8] Cheng Z.-L.a, Liu Z.b , Wan H.-L.c, *Chinese Journal of Chemistry*, Volume 23, Issue 1, January 2005, Pages 28-31
[9] Cheng Z.L., Chao Z.S., Wan H.L., *Chinese Chemical Letters*, Volume 14, Issue 8, 1 August 2003, Pages 874-876
[10] Di Renzo F., Fajula F., *Studies in Surface Science and Catalysis*, Volume 157, 2005, Pages 1-12
[11] http://www.ccsd.biz/publications/files/RR/RR%2091%20Manuf%20of%20lowgrade%20zeolite_web.pdf
[12] Ribeiro F.R. et. al., *Zeolites: Science and Technology*, Martinus Nijhoff Publishers, The Hague, 1984.
[13] Crupi et al., *Vibrational spectroscopy* 42 (2006), 375-380
[14] A. Alberti et al., *Microporous and Mesoporous Materials*, Volume 42, Issues 2-3, February 2001, Pages 277-287
[15] A. Zecchina et al., *J. Phys. Chem.;* 1996; 100(41); 16584-16599
[16] Takeuchi et al., *Appl. Cat. A* 307 (2006) 13

[17] Cho et al., *Chemometrics and Intelligent Laboratory Systems*, 82 (2006), 104-108)
[18] Buzea C., Pacheco I., Robbie K. (2007). *Biointerphases* 2 (4): MR17–MR71.;
[19] ASTM E 2456 – 06 Standard Terminology Relating to Nanotechnology
[20] Philip S. Rawson (1984). *Ceramics.* University of Pennsylvania Press.
[21] M.C.Daniel, D. Astruc, *Chem. Rev.* 2004, 104, 293-346)
[22] Faraday, Michael (1857). *Phil. Trans. Roy. Soc. London* 147: 145–181
[23] Turner, T. (1908). *Proc. Roy. Soc. Lond. A* 81 (548): 301.
[24] "Sunscreen". U.S. Food and Drug Administration. http://www.fda.gov/Radiation-EmittingProducts/RadiationEmittingProductsandProcedures/Tanning/ucm116445.htm
[25] Mitchnick, MA; Fairhurst, D; Pinnell, SR (1999). *Journal of the American Academy of Dermatology* 40 (1): 85–90
[26] "The Textiles Nanotechnology Laboratory", http://nanotextiles.human.cornell.edu/
[27] Sergey P. Gubin (2009). *Magnetic nanoparticles*. Wiley-VCH.
[28] Buffat, Ph.; Burrel, J.-P. (1976). *Physical Review A* 13 (6): 2287.
[29] Moon, K.S. et al, *Journal of electronic materials*, Volume 34, no 2, 2005
[30] Filon Larese et al. *Toxicology* 255 (2009) 33-37
[31] Nel, Andre; et al. (3 February 2006), *Science* 311 (5761): 622–7.
[32] Magrez, Arnaud; et al. (2006), *Nano Letters* 6 (6): 1121–5.
[33] http://www.silverinstitute.org/
[34] Lefort, T.E. Socie´te´ Françoise de Catalyse Generalise´e. FR 729 952, 1931; 739 562, 1931.

[35] Rebsdat, S.; Mayer, D. *Ullmann's Encyclopedia of Industrial Chemistry*, 5th ed.; VCH Publishers: New York, 1988; Vol. A10.

[36] Weissermel, K.; Arpe, H.-J. *Industrial Organic Chemistry*; Wiley-VCH: Weinheim, Germany, 1994

[37] Cavicchioli et al., *Materials Letters* 59 (2005) 3585-3589

[38] Dadosh t., *Materials Letters* 63 (2009) 2236-2238

[39] Brinker, C.J.; G.W. Scherer (1990). *Sol-Gel Science: The Physics and Chemistry of Sol-Gel Processing*. Academic Press

[40] Klein, L. (1994). *Sol-Gel Optics: Processing and Applications*. Springer Verlag

[41] Corriu R., Nguyên Trong Anh (2009). *Molecular Chemistry of Sol-Gel Derived Nanomaterials*. John Wiley and Sons

[42] J. Kimling, M. Maier, B. Okenve, V. Kotaidis, H. Ballot, and A. Plech, *J. Phys. Chem. B* 2006, 110, 15700-15707

[43] R. He, X. Qian, J. Yin, Z. Zhu, *J. Mater. Chem.* 12 (2002) 3783.

[44] Yamamoto, S., Fujiwara, K., Watari, H. S, *Analytical Sciences* 20 2004: pp. 1347 – 1352].

[45]] Xia, Y., Halas, N. J. Shape – controlled Synthesis and Surface, Plasmonic Properties of Metallic Nanostructures MRS Bulletin 30 2005: pp. 338 – 343.

[46] www.philiplaven.com/mieplot.htm

[47] *Analytica Chimica Acta* 496 (2003) 17–27

Acknowledgments

The Author would like to thank INSTM for having funded the present work in collaboration with University of Bologna.

The Author also thanks Prof. Alessandro Trovarelli from University of Udine and his collaborators Dr. Loredana de Rogatis and Dr. Eleonora Aneggi for the precious collaboration in catalytic tests on soot decomposition and Dr. Luca Gregoratti and all the beamline scientists of ESCAMicroscopy at ELETTRA synchrotron facility in Trieste.